Monthly Weather Review

VOLUME 98, NUMBER 3

MARCH 1970

UDC 551.513.1:556.1:551.509.313

SIMULATED CLIMATOLOGY OF A GENERAL CIRCULATION MODEL WITH A HYDROLOGIC CYCLE

III. Effects of Increased Horizontal Computational Resolution

SYUKURO MANABE, JOSEPH SMAGORINSKY, J. LEITH HOLLOWAY, JR., and HUGH M. STONE

Geophysical Fluid Dynamics Laboratory, ESSA, Princeton, N.J.

ABSTRACT

The results of a numerical time integration of a hemispheric general circulation model of the atmosphere with moist processes and a uniform earth's surface has already been published by Manabe, Smagorinsky, and Strickler. In this study, the integration is repeated after halving the midlatitude grid size from approximately 500 to 250 km.

This increase in the resolution of the horizontal finite differences markedly improves the features of the model atmosphere. For example, the system of fronts and the associated cyclone families in the high resolution atmosphere is much more realistic than that in the low resolution atmosphere. Furthermore, the general magnitude and the spectral distribution of eddy kinetic energy are in better agreement with the actual atmosphere as a result of the improvement in resolution.

In order to explain these improvements, an extensive analysis of the energetics of both the low and high resolution atmospheric models is carried out. It is shown that these improvements are due not only to the increase of the accuracy of the finite differences but also to the shift in the scale of dissipation by the nonlinear lateral viscosity toward a smaller scale resulting from the decrease in grid size. In the low resolution atmospheric model, the transfer of energy from eddy to zonal kinetic energy is missing because of excessive subgrid scale dissipation at medium wave numbers, whereas it has significant magnitude in the high resolution atmospheric model. It is speculated that further increase of resolution should improve the results because it tends to separate the characteristic scale of dissipation from that of the source of eddy kinetic energy.

The analysis of the energetics in wave number space clearly demonstrates the differences between the energetics of the different parts of the atmosphere. In middle latitudes there are essential differences between the energetics of the model troposphere and that of the model stratosphere. In the model troposphere, the eddy kinetic energy is produced by the conversion of eddy potential energy in the range of wave numbers from 2 to 8. Part of the energy thus produced is dissipated by the subgrid scale dissipation, and most of the remainder is decascaded to zonal kinetic energy. In the model stratosphere, where very long waves predominate, the eddy kinetic energy is generated in the range of wave numbers from 2 to 3 by the energy supplied from the troposphere. Most of this energy is then decascaded barotropically to zonal kinetic energy.

In the Tropics, eddy kinetic energy is mainly produced by the release of eddy available potential energy generated by the heat of condensation. Although the rate of conversion is maximum at very low wave numbers, the conversion spectrum extends to very high wave numbers.

A box diagram of the energetics of the high resolution moist model shows that the eddy available potential energy is generated by the heat of condensation as well as by energy transfer from the zonal available potential energy. Furthermore, it is noteworthy that the zonal kinetic energy is maintained not only by the barotropic exchange from the eddy kinetic energy but also from the conversions of zonal potential energy. The intensification of the direct tropical cell and the weakening of the indirect Ferrel cell in middle latitudes caused by the moist processes are responsible for this positive zonal conversion.

One of the highlights of the results from the integration of the high resolution moist model is the successful simulation of the evolution of fronts and the associated cyclone families. The influence of moist processes upon frontal structure as well as other synoptic features is investigated by comparing the moist model atmosphere with the dry model atmosphere without the effect of the selective heating of condensation. It is found that the heat of condensation significantly reduces the width of fronts and the characteristic scale of cyclones in the lower troposphere.

CONTENTS

1. INTRODUCTION

This study is a continuation of "Simulated Climatology of a General Circulation Model With a Hydrologic Cycle." Hereafter, we shall refer to part 1 (Manabe et al. 1965) as study M and part 2 (Manabe and Smagorinsky 1967) as study M2 for ease of identification.

In study M, a numerical experiment of the general circulation of the atmosphere was carried out taking into consideration interactions with the hydrologic cycle. The state of quasi-equilibrium was obtained by numerical integration of the primitive equations of motion, the thermodynamical equation, and the prognostic equation of specific humidity. The radiative flux was computed from the equation of radiative transfer assuming the climatological distribution of water vapor, carbon dioxide, ozone, and cloud. The solar radiation at the top of the model atmosphere was assumed to have the annual mean distribution. The hydrological part of the model consisted of the advection of water vapor by the large-scale motion, evaporation from the earth's surface, precipitation, and a convective adjustment of temperature and moisture. The temperature of the earth's surface was determined from a condition of heat balance at the earth's surface, which was assumed to be a completely wet and flat surface with zero heat capacity. For further details of the model structure, see also the study of the general circulation model without the hydrologic cycle (Smagorinsky et al. 1965). Hereafter, we shall refer to this paper as study S.

Quasi-equilibrium was obtained as an asymptotic state emerging from the numerical time integration of the model atmosphere. The initial condition for this time integration was an isothermal and dry atmosphere at rest. In order to economize computer time, a very coarse grid size was chosen at the beginning of the time integration, and the resolution was refined stepwise as the integration proceeded. It was our original intention to keep refining the resolution until the large-scale motion field was sufficiently resolved and the result insignificantly altered by further refinement. However, in these studies we stopped at a grid size of 500 km because of the limitation of computer time despite the, as yet, significant dependence of the results upon refinement. Nevertheless, the state of quasi-equilibrium which emerged from this integration has various features common with the actual atmosphere, such as the tropical rain belt, the subtropical dry belt, and the middle-latitude rain belt. Furthermore, the thermal structure of the joint troposphere-stratosphere system and the latitudinal gradient of the tropopause height were successfully simulated. There are, however, various features of the model which require further improvement. For example, the finite-difference mesh with a grid size of 500 km is not capable of satisfactorily resolving frontal structure and associated cyclones. According to study M, the heat of condensation tends to reduce the scale of the flow patterns near the earth's surface. With respect to the characteristic scale of surface cyclone systems, the moist model atmosphere more closely matches the real atmosphere than does the dry model atmosphere. Detailed analysis of synoptic systems of the moist model atmosphere reveals that the 500-km grid is far from sufficient to resolve the flow patterns near the earth's surface and indicates the need for further increases in the resolution of the horizontal finite differencing.

Another unrealistic feature of the low resolution moist model atmosphere was the small magnitude of the eddy kinetic energy. The magnitude of the eddy kinetic energy in the moist model atmosphere was much smaller than in the actual atmosphere. An analysis of experimental weather predictions performed with a similar model (Smagorinsky and Staff Members 1967, Miyakoda et al. 1969) indicated that improvement in horizontal resolution increased the level of eddy kinetic energy and markedly improved the quality of the dynamical prediction. Since the nonlinear viscosity proposed by Smagorinsky (1963) is proportional not only to the absolute value of the vertical component of deformation but also to the square of the grid size, it is probable that the improvement in resolution of the horizontal finite differences affects the spectral distribution of dissipation as well as the accuracy of horizontal finite differencing, that is, it decreases the scale of dissipation. As a result of the availability of a faster computer, it was decided to repeat study M with double horizontal resolution in an attempt to improve the simulation of the dynamical structure of the atmosphere. In the new study, special emphasis is placed upon an analysis of the budget of eddy kinetic energy in wave number space in order to determine how the change of resolution affects the energetics and the energy spectrum of the model atmosphere. Since many earlier numerical simulations of the general circulation have been conducted with a coarse grid system, the present study can be useful for reevaluating the previous results of these experiments. Moreover, a study of the energetics in wave number space can be useful for establishing how the spectrum of eddy kinetic energy is maintained in a moist atmosphere. Special emphasis will be placed upon a comparison between the energetics in the stratosphere vis-à-vis the troposphere and in the middle latitudes vis-à-vis the Tropics.

Another objective of this study is the construction of a box diagram of the energy budget in the high resolution moist model atmosphere. The energetics of the dry model atmosphere has been extensively investigated by Phillips (1956), Smagorinsky (1963), Smagorinsky et al. (1965, study S). However, the energetics of a moist model atmosphere has hardly been explored. In a dry atmosphere, the eddy available potential energy is solely supplied by energy transfer from zonal to eddy available potential energy. However, the preliminary study of the moist model with coarse resolution (M2) indicated that the heat of condensation could also be responsible for the generation of eddy available potential energy. In a dry model atmosphere, there is a small conversion of zonal kinetic energy into zonal potential energy. According to the

preliminary study (M2), the sense of the conversion could be reversed in the moist atmosphere because of the intensification of the direct tropical cell of the meridional circulation resulting from the release of the heat of condensation. Since it is very difficult to determine the distribution of the release of heat of condensation and of the meridional circulation in the actual atmosphere, the magnitudes of the zonal conversion and the eddy generation of available potential energy are not certain. Under these circumstances, it is very useful to evaluate the contribution of these effects in the moist model atmosphere provided that the model atmosphere is sufficiently similar to the actual atmosphere in other verifiable characteristics.

2. BRIEF DESCRIPTION OF THE MODEL

The structure of this high resolution model is identical with that of the low resolution model described in the previous study M. Therefore, it will be explained only very briefly here.

Assuming the hydrostatic relationship and adopting pressure normalized by surface pressure as the vertical coordinate, we can write the equations of motion in λ (longitude), θ (latitude), and σ (normalized pressure) coordinates as

$$\frac{\partial}{\partial t}(P_* u) = -\mathcal{D}_3(u) + \sin\theta \cdot (\dot{\lambda}+2\Omega)\cdot(P_* v) - R\frac{\partial(P_* T)}{a\cos\theta\partial\lambda} - \frac{\partial}{\partial\sigma}\left(P_*\sigma\frac{\partial\phi}{a\cos\theta\partial\lambda}\right) + F_\lambda \quad (1)$$

and

$$\frac{\partial}{\partial t}(P_* v) = -\mathcal{D}_3(v) - \sin\theta \cdot (\dot{\lambda}+2\Omega)\cdot(P_* u) - R\frac{\partial(P_* T)}{a\partial\theta} - \frac{\partial}{\partial\sigma}\left(P_*\sigma\frac{\partial\phi}{a\partial\theta}\right) + F_\theta \quad (2)$$

where a is the radius of the earth, R is the gas constant, P is pressure, P_* is the surface pressure, $u = a\cos\theta\cdot\dot{\lambda}$, $v = a\dot{\theta}$, $\sigma = P/P_*$, Ω is the angular velocity of the earth, T is temperature, ϕ is the geopotential of a σ-surface, F_λ and F_θ are frictional forces in the zonal and the meridional directions, respectively, and

$$\mathcal{D}_3(\ ) = \frac{\partial((\ )P_* u)}{a\cos\theta\partial\lambda} + \frac{\partial((\ )P_* v\cos\theta)}{a\cos\theta\partial\theta} + \frac{\partial((\ )P_*\dot{\sigma})}{\partial\sigma}. \quad (3)$$

The first law of thermodynamics is

$$\frac{\partial}{\partial t}(P_* T) = -\mathcal{D}_3(T) + \frac{R}{c_p}\frac{T\omega}{\sigma} + \frac{P_*\dot{q}}{c_p} + F_T \quad (4)$$

where c_p is the specific heat capacity at constant pressure, ω is vertical P-velocity (dP/dt), and $\dot{q}$ is heat added per unit mass by radiation and condensation, and F_T is the effect of thermal diffusion. The continuity equation may be written as

$$\frac{\partial}{\partial t}P_* = -\mathcal{D}_3(1). \quad (5)$$

The hydrostatic relation is

$$\frac{\partial\phi}{\partial\sigma} = -\frac{RT}{\sigma}. \quad (6)$$

The prognostic equation of the mixing ratio of water vapor is

$$\frac{\partial}{\partial t}(P_* r) = -\mathcal{D}_3(r) - P_* C + F_r \quad (7)$$

where r is the mixing ratio of water vapor, C is the rate of condensation, and F_r is the change of mixing ratio due to the subgrid scale eddy diffusion. These equations were rewritten in the stereographic projection system and numerically integrated in a hemispheric domain. A free-slip insulated wall is placed at the Equator, and a flat and wet earth's surface without any heat capacity is imposed as the lower boundary condition. Figure 1 is a schematic diagram of the structure of the moist model and indicates that computation of the radiative transfer and of hydrologic changes yield the values of $\dot{q}$ and C, respectively. The details of these computations and the description of the coupling among the various components of the model can be found in M. In order to identify the interactions of the hydrologic process, the moist model atmosphere is often compared with the dry model in this study. Further details of the structure of the dry model which lacks moisture advection and condensation can be found in study S.

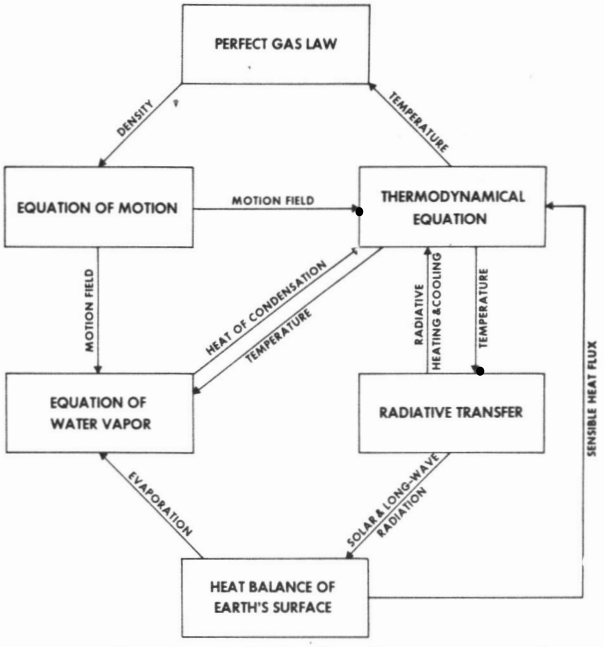

FIGURE 1.—Box diagram indicating the structure of the model.

Since we shall discuss how the horizontal (subgrid scale) eddy viscosity affects the circulation of the moist model atmosphere depending upon the resolution of horizontal finite differencing, we need to briefly describe the formulation of the nonlinear viscosity proposed by Smagorinsky (1963). The zonal and meridional components of the frictional forces may be written as the sum of the derivatives of stress tensors in the following way:

$$F_\lambda=\frac{P_*}{\rho}\left[\frac{\partial \tau^{\lambda\lambda}}{a\cos\theta\partial\lambda}+\frac{\partial \tau^{\lambda\theta}\cos^2\theta}{a\cos^2\theta\partial\theta}+\frac{\partial \tau^{\lambda z}}{\partial z}\right] \tag{8}$$

and

$$F_\theta=\frac{P_*}{\rho}\left[\frac{\partial \tau^{\lambda\theta}}{a\cos\theta\partial\lambda}+\frac{\partial \tau^{\theta\theta}\cos\theta}{a\cos\theta\partial\theta}+\frac{\tan\theta}{a}\tau^{\lambda\lambda}+\frac{\partial \tau^{\theta z}}{\partial z}\right] \tag{9}$$

where ρ is the density of air, $\tau^{\lambda\lambda}$, $\tau^{\lambda\theta}$, $\tau^{\theta\lambda}$, and $\tau^{\theta\theta}$ denote the stress tensors resulting from horizontal mixing, and $\tau^{\lambda z}$ and $\tau^{\theta z}$ denote those from vertical mixing. Assuming that the stress tensors can be expressed by a linear combination of strain tensors and imposing the hydrostatic requirement, the following relationship for two-dimensional isotropic turbulence results:

$$\tau^{\lambda\lambda}=-\tau^{\theta\theta}=\rho\gamma_H D_T \tag{10}$$

and

$$\tau^{\lambda\theta}=\tau^{\theta\lambda}=\rho\gamma_H D_S \tag{11}$$

where

$$D_T=\frac{\partial u}{a\cos\theta\partial\lambda}-\frac{\cos\theta}{a}\frac{\partial}{\partial\theta}\left(\frac{v}{\cos\theta}\right) \tag{12}$$

and

$$D_S=\frac{\partial v}{a\cos\theta\partial\lambda}+\frac{\cos\theta}{a}\frac{\partial}{\partial\theta}\left(\frac{u}{\cos\theta}\right). \tag{13}$$

The assumption of an inertial subrange yields through dimensional analysis that

$$\gamma_H=l^2|D| \tag{14}$$

where $|D|=[D_T^2+D_S^2]^{1/2}$ and l is a characteristic length corresponding to the scale defining the exchange coefficient. This length is assumed to be

$$l=k_0\left(\frac{d}{\sqrt{2}}\right)=0.28d \tag{15}$$

where d is the grid size and k_0 is the Kármán constant. Based upon spectral measurements of Pond et al. (1963), Lilly (1966) estimated the value of l to be 0.23 d, which is close to what is used here.

In the following discussions, the horizontal resolution will be identified by N, that is, the number of grid points between the Pole and the Equator. Accordingly, the grid size of the high resolution grid will be identified as *N40* and that of the low resolution grid as *N20* (table 1). The capital letters M and D will denote the moist and the dry model, respectively. See appendix II for a brief description of the dry model.

3. TIME INTEGRATION

The initial condition for the numerical time integration of the *N40M* model atmosphere was the state which was reached after 150 days in the time integration of the models with coarser resolutions. Table 2 shows the specific horizontal resolution at various stages of the integration. The value of N was increased stepwise from 5 to 10, to 20, and then to 40. Since the computer time required for the numerical time integration is proportional to N^3, this method of integration significantly reduces the amount of computation for reaching the state of quasi-equilibrium. Further details of the method of numerical time-integration may be found in appendix I.

TABLE 1.—*Latitudinal dependence of grid size for the high and low resolution grids*

	Grid size (km)	
	N40	*N20*
Equator	160	320
40° latitude	270	540
Pole	320	640

TABLE 2.—*Horizontal resolution used in the integration of the N40M atmosphere*

Resolution	Period of integration
$N=5$	0–50th day
$N=10$	50–70th day
$N=20$	70–210th day
$N=40$	150–230th day

The initial condition for the *N5M* model is an isothermal, completely dry, and resting atmosphere. The time evolution of the hemispheric average value of the total potential energy, and of the gross static stability are shown in figure 2. Similar graphs for precipitable water, rate of precipitation, and rate of evaporation are shown in figure 3. The time evolution of total kinetic energy and of relative and absolute angular momentum are shown in figure 4. These figures clearly demonstrate that the atmosphere is sufficiently close to a state of quasi-equilibrium toward the end of the integration. The period of analysis chosen for this study is the last 30 days of the *N40M* integration, that is, from the 200th to the 230th day. The data, which are shown in the following section are obtained by taking the time mean for this 30-day period.

4. TIME MEAN FIELD

A. ZONAL WIND FIELD

In figure 5, the latitude-height distribution of the zonal wind of the *N40M* model and *N20M* model are compared with that of the actual atmosphere. General features of the distributions of the two models are very similar, and the intensity of the westerlies in both model atmospheres is much stronger than in the actual atmosphere. A similar tendency for strong westerlies was evident in the model atmospheres of Phillips (1956) and Smagorinsky (1963). The reason for such a tendency is not obvious. This seems to be one of the most fundamental discrepancies between the features of model atmospheres and those of the actual atmosphere.

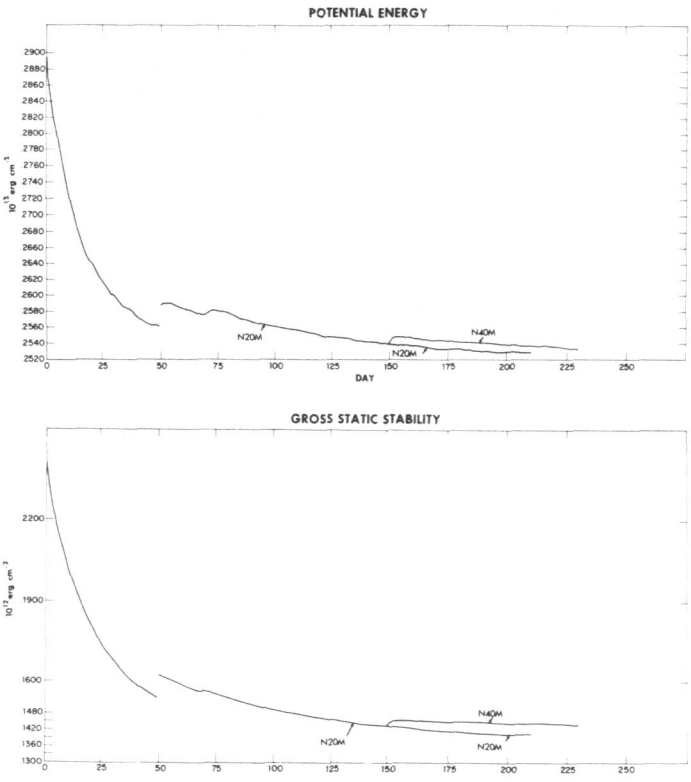

FIGURE 2.—Time variation of various hemispheric mean quantities. Upper graph, total potential energy; lower graph, gross static stability. See appendix 2c of study S for the definition of gross static stability.

A detailed comparison between the zonal wind fields of the two models (*N20M* and *N40M*) reveals the following changes which resulted from the increase in the resolution of the horizontal finite differencing:

1) A poleward shift of 5° latitude of maximum tropospheric zonal wind. This is still equatorward of the position of the maximum in the actual atmosphere.

2) The development of surface easterlies in the polar region.

B. MERIDIONAL CIRCULATION

The stream functions of the meridional circulation in the *N40M* atmosphere and in the *N20M* atmosphere are shown in figure 6. In the troposphere of both models, there are three cells, that is, the direct cell of the Tropics, the indirect cell in middle latitudes, and the direct cell of the polar region. These cells are characterized by a shallow layer of intense mass transport in the planetary boundary layer and a return flow mainly in the upper troposphere. In both model stratospheres there are two major cells and a very weak indirect cell at the Equator. With information based upon a study of the budget of angular momentum, Teweles (1963) computed the meridional circulation in the actual atmosphere, obtaining two major circulation cells similar to those shown in figure 6. Miyakoda (1963) also obtained two major cells for the winter season by solving the "ω-equation." The existence of a weak indirect cell in the actual equatorial stratosphere is not certain, although Wallace (1967) suggested the existence of downward motion in the tropical stratosphere based upon a study of the budget of angular momentum.

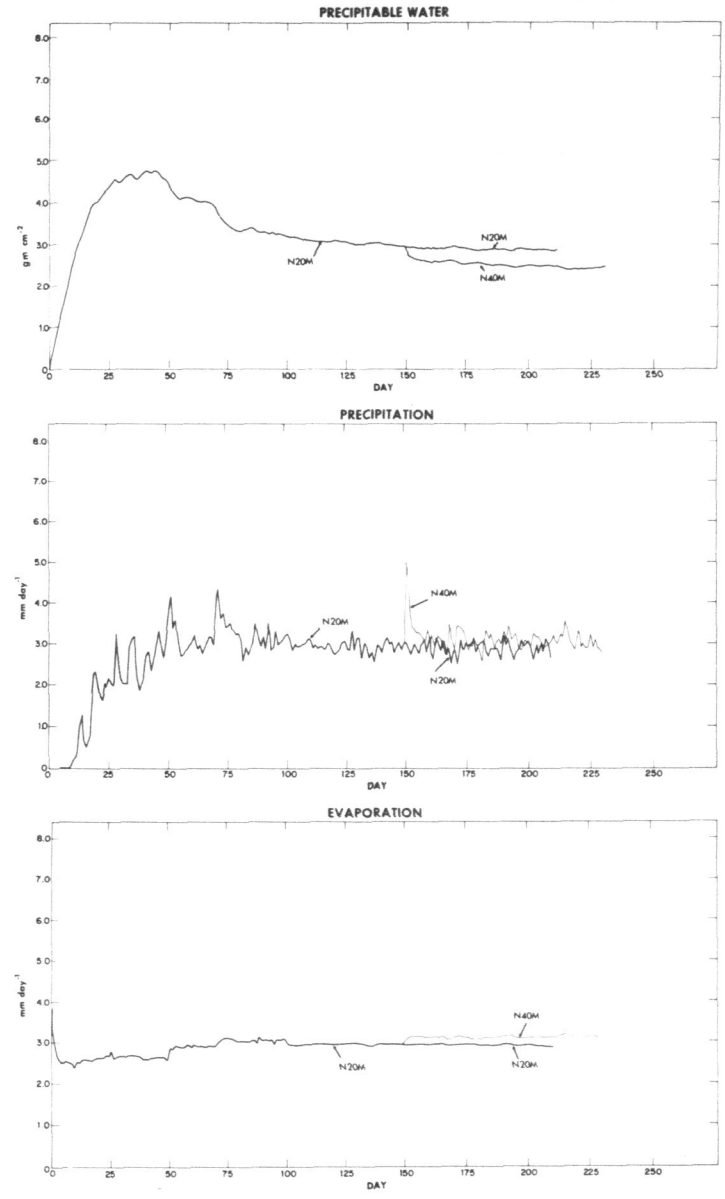

FIGURE 3.—Time variation of various hemispheric mean quantities. Upper graph, precipitable water; middle graph, rate of precipitation; lower graph, rate of evaporation.

If one compares the intensities of the meridional circulation in the two model atmospheres, one finds that the indirect cell of middle latitudes in the *N40M* atmosphere is about one and a half times stronger than in the *N20M* atmosphere. According to figure 7, which shows the latitudinal distributions of the zonal mean surface pressure in both models, the meridional gradient of the surface pressure in middle latitudes increases with increased resolution. This increase probably is responsible for the difference in the intensity of the indirect cell. Phillips (1954) has shown that baroclinically unstable waves are responsible for driving the indirect cell. As it will be shown in the following section, the magnitude of the eddy kinetic energy in the *N40M* atmosphere is larger than that in the *N20M* atmosphere. Therefore, it is reasonable that

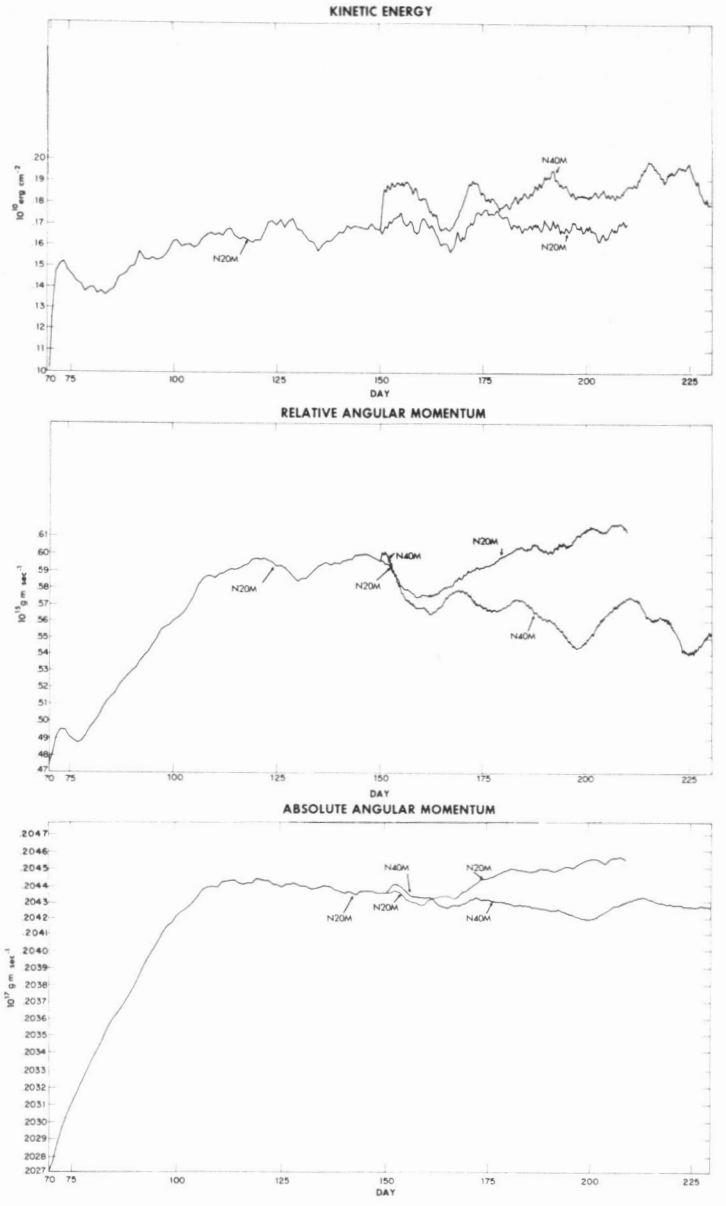

FIGURE 4.—Time variation of various hemispheric mean quantities. Upper graph, total kinetic energy; middle graph, relative angular momentum; lower graph, absolute angular momentum.

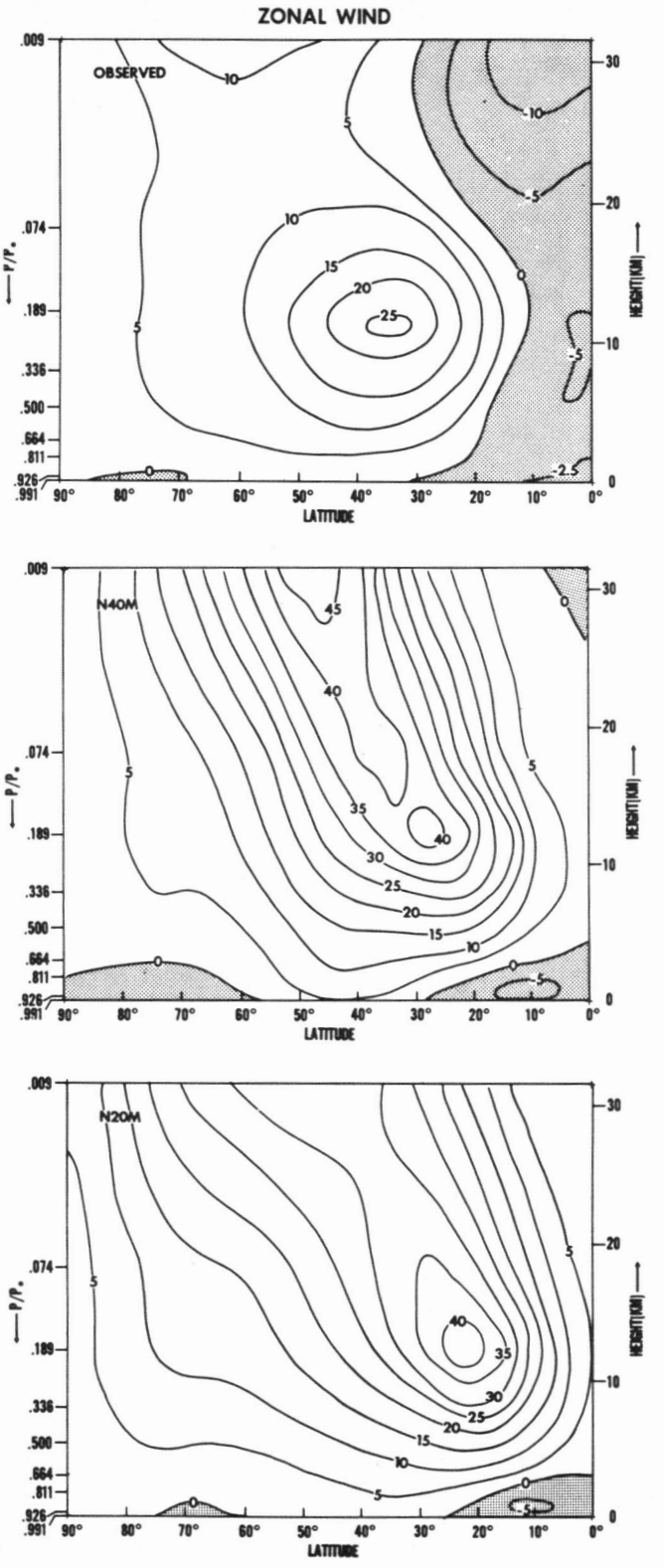

FIGURE 5.—Zonal mean of zonal wind in the various atmospheres. Upper distribution, actual atmosphere (data source, Rasmusson and Oort 1970 and Batten 1964); middle distribution, the *N40M* model; lower distribution, the *N20M* model. Units, m sec^{-1}.

the indirect meridional circulation in the former is more intense than that in the latter.

The latitude-height distributions of the meridional component of the wind and vertical P-velocity (ω) in the *N40M* atmosphere are shown in figure 8.

C. EDDY KINETIC ENERGY

The latitude-height distributions of the zonal mean value of the eddy kinetic energy in both the *N40M* and the *N20M* atmospheres are shown in figure 9. In both models, the height of the maximum eddy kinetic energy lies in the upper troposphere in agreement with the features of the actual atmosphere. The magnitude of the eddy kinetic energy of the *N40M* model, however, is quite different from that of the *N20M* model. In middle latitudes, the former is about twice as large in the stratosphere. As we shall see in the following section, this difference is caused partly by the decrease of the effective viscosity

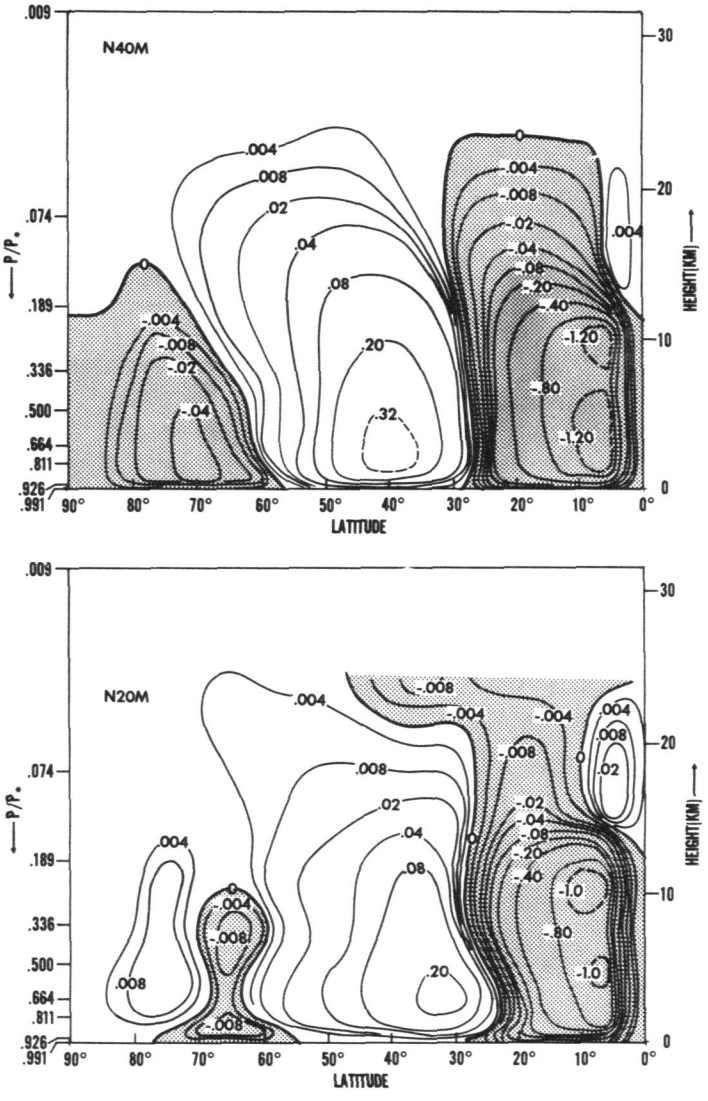

FIGURE 6.—Stream functions of meridional circulation; area of counterclockwise circulation is shaded. Upper half, the *N40M* model; lower half, the *N20M* model. Units, 10^{14} gm sec^{-1}.

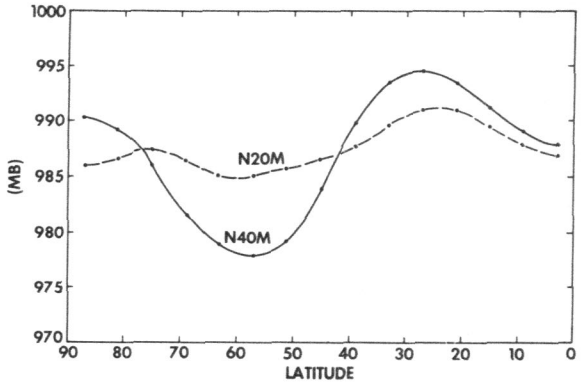

FIGURE 7.—Latitudinal distribution of the zonal mean of surface pressure. Without mountains these models have mean sea level pressures about 25 mb lower than the actual atmosphere.

and partly by the increase of the conversion of eddy potential energy. Both of these changes result from the increase of the horizontal resolution.

Figure 10 compares the distributions of eddy kinetic energy in the model atmospheres at 500 mb with those in the actual atmosphere estimated by Saltzman (1962).[1] Figure 10 clearly indicates that the magnitude of the eddy kinetic energy of the *N40M* model is closer to observed than that of the *N20M* model.

D. ENERGY SPECTRUM

In figure 11, the spectra of the eddy kinetic energy of both models at various isobaric surfaces are shown together with the annual mean spectrum in the actual atmosphere which was estimated by Teweles (1963). According to this figure, the magnitudes of the spectral components of the *N40M* model are significantly higher than those of the *N20M* model at all wave numbers and are closer to those estimated for the actual atmosphere. Originally, it was speculated that the energy spectrum of the lower wave numbers depended only slightly on the computational resolution because the nonlinear viscosity should only influence the higher wave numbers. This figure, however, indicates that energy of the lower wave numbers increased more than did that of the higher wave numbers as a result of the increase in the resolution. Hence, the general increase of the kinetic energy with decreasing wave number evident in Teweles' result is successfully simulated by the *N40M* model but not by the *N20M* model.

In order to compare the characteristic scale of the motion in the two models, we define an effective wavelength

$$L_{eff}=\frac{2\pi a\cos\theta}{\overline{n}} \tag{16}$$

where

$$\overline{n}=\frac{\int_0^\infty n\cdot dE(n)}{\int_0^\infty dE(n)}, \tag{17}$$

a=radius of the earth, and θ=latitude.

Here, $E(n)$ denotes the vertical mean kinetic energy of the component with wave number n. In figure 12, L_{eff} is plotted as a function of latitude. We see that the characteristic scale of motion definitely increases in middle latitudes and in the subtropics, resulting from the increase of horizontal resolution. This increase is consistent with the increase of the kinetic energy of the larger scale motion mentioned above. In subsection 6B, the reason for the difference between the energy spectra of the two models will be discussed extensively.

E. TEMPERATURE AND RELATIVE HUMIDITY

The latitude-height distributions of the zonal mean temperature and the zonal mean relative humidity in the *N40M* atmosphere are shown in figures 13 and 14, respectively. They differ slightly from the corresponding distri-

[1] Note that Saltzman (1962) used geostrophic wind for his study. Therefore, it is probable that his estimate may be too high.

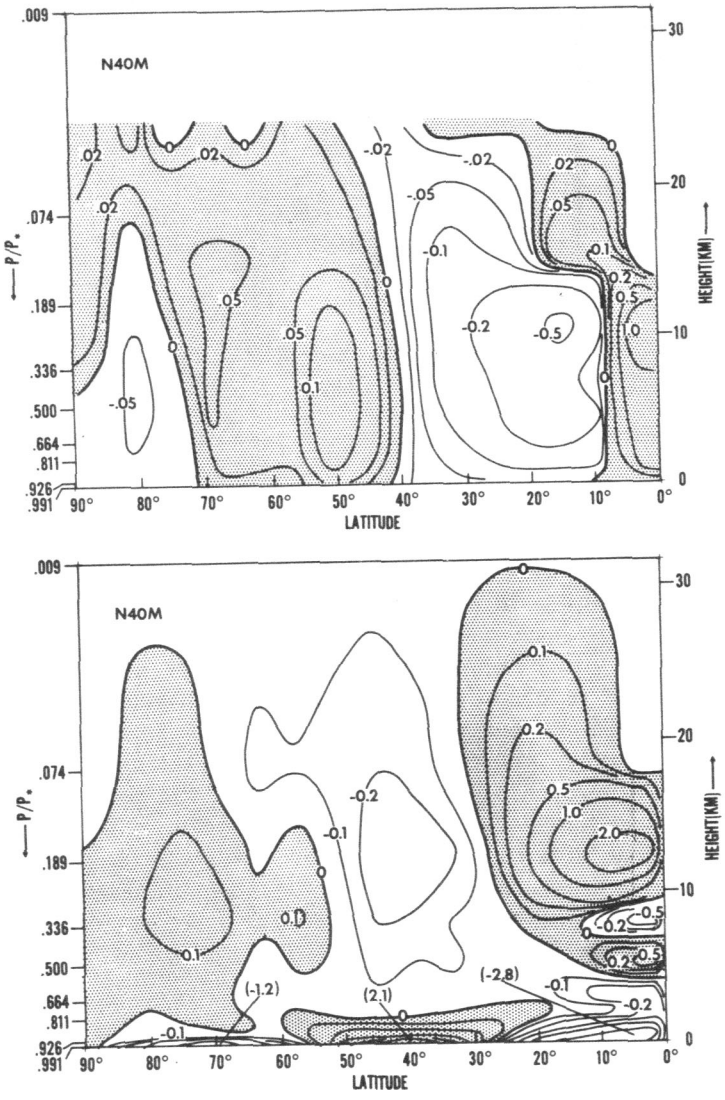

FIGURE 8.—Latitude-height distribution of the zonal mean currents in the *N40M* atmosphere. Upper half, vertical P-velocity (cm sec^{-1}); lower half, meridional component of wind (m sec^{-1}).

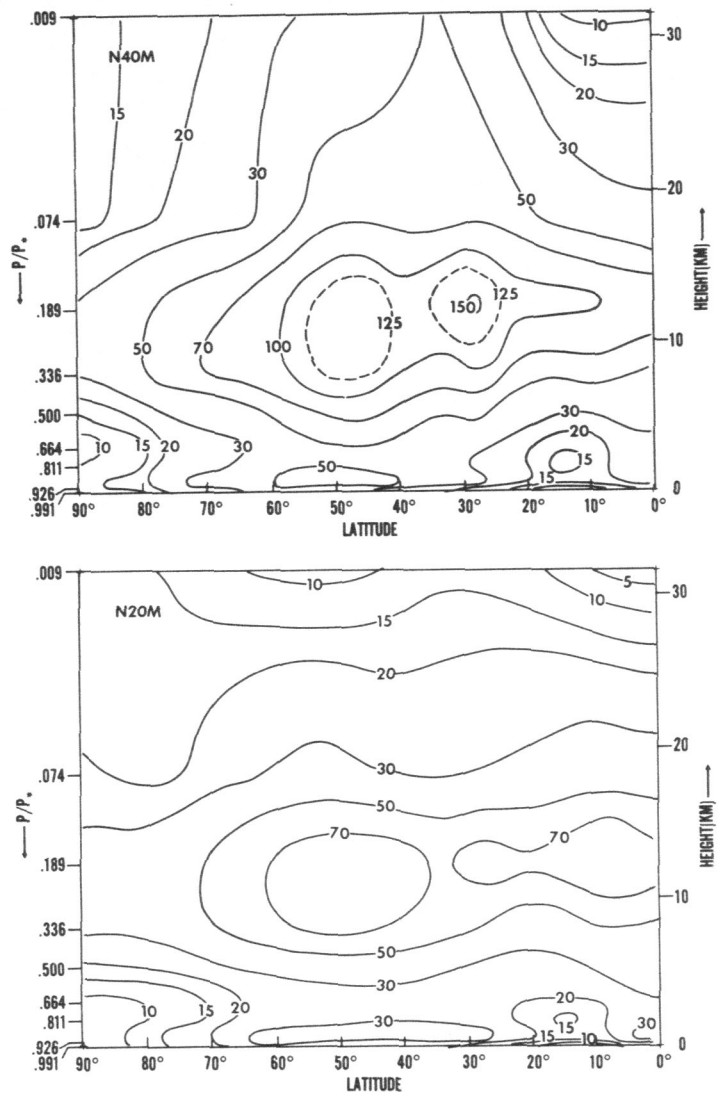

FIGURE 9.—Latitude-height distribution of the zonal mean value of eddy kinetic energy. Upper half, the *N40M* model; lower half, the *N20M* model. Units, 10^{-3} joules cm^{-2} mb^{-1}.

butions in the *N20M* atmosphere. The *N20M* distributions were already discussed in study M.

5. FRONT AND CYCLONE FAMILIES

In order to discuss the synoptic features of both moist atmospheric models, for each resolution the maps of daily precipitation, surface pressure, surface temperature at level 9 ($P \approx 991$ mb), and geopotential height at the 500-mb level on model day 173 are shown in figures 15 through 18. In the *N40M* atmosphere, narrow spiral bands of frontal rain extend from high to very low latitudes. In figure 19, which shows a TIROS picture of the Southern Hemisphere, spiral bands of cloud extend counterclockwise toward the Equator, suggesting the existence of rain bands with similar features in the actual atmosphere. As figures 16 and 17 indicate, fronts in the *N40M* atmosphere are also characterized by a very dense concentration of isotherms and are accompanied by cyclone families near the earth's surface.

In the low resolution *N20M* atmosphere, the rain bands are much wider and less distinct than in the *N40M* atmosphere. Also, the concentration of the isotherms is somewhat less in the *N20M* than in the *N40M* model, as is evident in figure 17. In short, the general features of the surface front become much more realistic as a result of doubling the resolution of horizontal finite differencing. Obviously, the coarse horizontal resolution of the *N20M* model is not sufficient to resolve the frontal structure.

We have shown the synoptic maps of both the *N20* and the *N40* atmosphere and pointed out that the general features of the frontal systems in the *N40M* atmosphere are much more realistic than those in the *N20M* atmosphere. It would now be instructive to follow the time evolution of these simulated fronts in the *N40M* atmosphere and

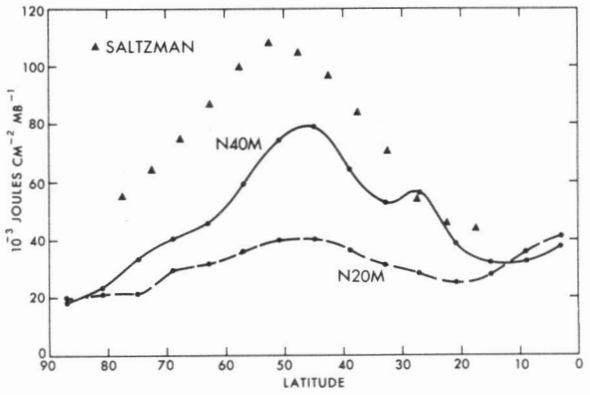

FIGURE 10.—Mean latitudinal distribution of eddy kinetic energy at the 500-mb level. (Actual atmosphere, Saltzman 1962; geostrophic wind approximation is used for this estimate.)

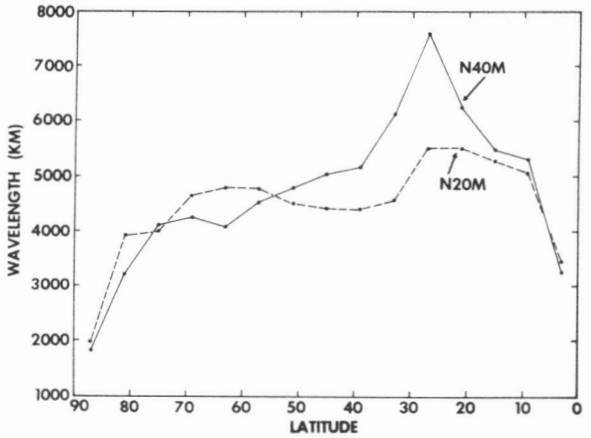

FIGURE 12.—Latitudinal distribution of the average mean effective wavelength.

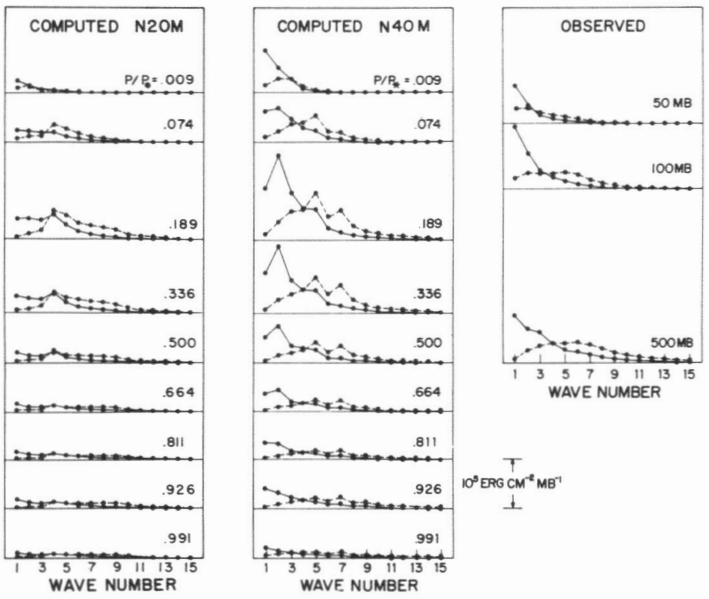

FIGURE 11.—Mean spectra of eddy kinetic ebergy of the region from 15° to 81° latitude at various isobaric surfaces in the *N20M* and *N40M* models and in the actual atmosphere (Teweles 1963). The spectra of eddy kinetic energy of the zonal and meridional components of the wind are shown by solid and dashed lines, respectively.

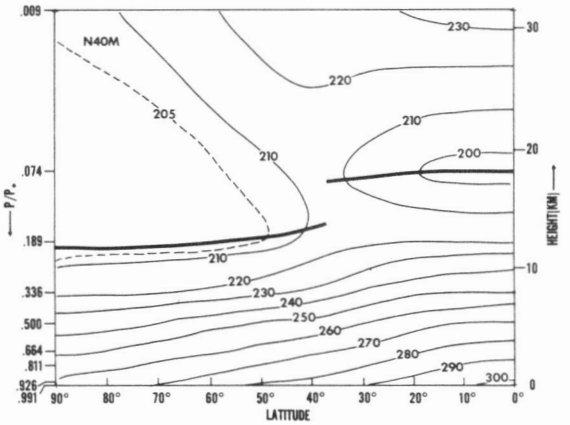

FIGURE 13.—Latitude-height distribution of the zonal mean temperature of the *N40M* atmosphere. Units, °K.

carry out a detailed analysis of their structure. A standard synoptic frontal analysis was made daily for the *N40M* model atmosphere during the period from day 167 to day 177. Pressure, temperature, and wind fields were used to determine frontal locations. Figures 20 and 21 show part of this analysis for alternate days. They give maps of surface pressure, precipitation, wind, and temperature at level 9 ($P/P^*=0.991$). All scalar fields in this figure were analyzed by machine, and the wind vectors were drawn by machine. The frontal analysis is the only operation done subjectively by hand.

The development of two frontal systems can be followed during this period. Frontogenesis is indicated for one system in the upper left-hand corner of the map at the 167th day; the other system on this day is a weak open wave. Along the front in the upper left-hand corner, one can identify three cyclones denoted by LA, LB, and LC, which resemble a typical cyclone family in the actual atmosphere. These cyclones move northeastward and go through a typical life cycle. For example, cyclone LC is barely detectable on the 167th day. It keeps developing until the 173d day. On the 175th day, the occlusion process is completed, and the cyclone starts decaying very rapidly. Another frontal system on the right-hand side undergoes a similar evolution. The evolution of the front and the associated cyclone described here is quite similar to that observed in the actual atmosphere (see also, Miyakoda et al. 1969). Furthermore, the temperature gradient, wind shifts, and rainfall in the vicinity of these model fronts are highly realistic. In general, the change of direction of the surface wind vector is not very abrupt across a warm front. However, large wind

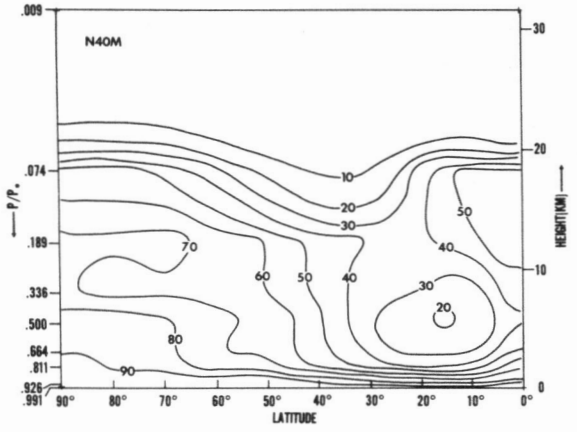

FIGURE 14.—Latitude-height distribution of the zonal mean relative humidity of the *N40M* atmosphere.

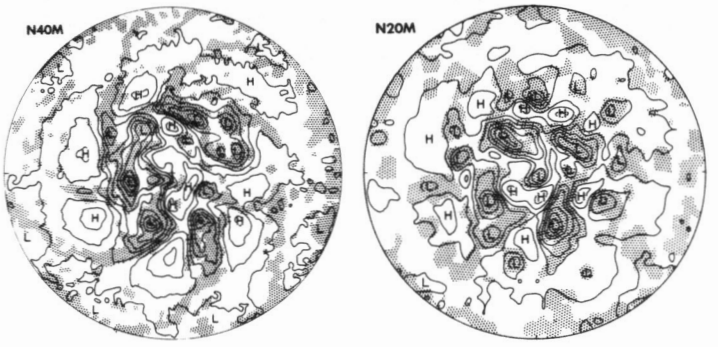

FIGURE 16.—Stereographic map of surface pressure on model day 173. Contour interval is every 5 mb. Shading indicates area of precipitation in excess of 0.1 cm day^{-1}; circular boundary, Equator.

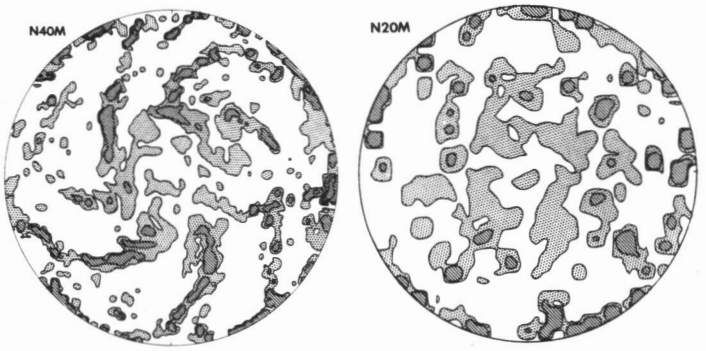

FIGURE 15.—Stereographic map of daily precipitation (cm day^{-1}) on model day 173. Shading indicates areas of precipitation; slashed-line shading, area of daily precipitation in excess of 1.0 cm day^{-1}; dotted shading, area of daily precipitation in excess of 0.1 cm day^{-1}; circular boundary, Equator.

shear is evident across the cold front, in agreement with the features of the actual atmosphere.

The cross sections presented in figure 22 were made through the model fronts on day 173. Their locations are indicated in figure 21 by heavy lines marked A–B, C–D, and E–F. The top, middle, and bottom rows of figure 22 show the wind component normal to the cross section, the vertical motion, and the relative humidity, all superimposed upon temperature.

In cross-section A–B, which cuts the cold and warm fronts through the warm sector of the wave, upward vertical motion is strong in the warm sector with weak downward motion in the cold air behind the cold front and ahead of the warm front. Upward-moving air is moist, and downward-moving air is dry. The slope of the cold front is steeper than the slope of the warm front, in agreement with characteristics of the actual atmosphere. The jet stream is located above the cold front, where the horizontal temperature gradient is strongest. It is similar to cross sections through the real atmosphere (for example, Bjerknes 1951). Fronts on the cross sections were drawn on the basis of temperature gradient only. They are not as distinct as real fronts because of the still rather coarse spatial resolution of the model. A temperature inversion is analyzed through the warm front because the inversion does exist at the adjacent grid points.

Cross section C–D is placed through the cold high-pressure region and connects the two frontal systems. Upward vertical motion is located over all three fronts in this cross section, with weak downward motion directly above the cold dome of air and between the primary and secondary cold fronts. The secondary cold front began forming on day 171 when a cold mass of polar air began pushing southward. By day 173, the surface temperature gradient is quite strong behind this secondary front, even stronger than behind the primary front. The cross section shows that the primary front, although weak at the surface, extends high into the troposphere, above the 500-mb level, while the secondary front is rather shallow. This results in strong upward motion and heavy rain associated with the primary front. The two distinct rain bands can be seen on the map for day 173. Note that the slope of the cold front is steeper than that of the warm front, as was previously pointed out.

The cross section E–F intersects the cold front at about 20° latitude, which is quite far south for a front to be located; however, the surface temperature gradient is still strong here. The cross section shows that the front is shallow with a gradual slope; the vertical motions associated with it are weak. Weak downward motion appears in the cold air behind the front.

All three cross-sections shown here resemble cross sections through fronts in the real atmosphere. Although further increase in the resolution of the vertical and horizontal finite differences is desirable, it is clear that the *N40M* model is capable of reproducing the evolution and the structure of fronts and associated cyclone families.

Edelman (1963) has shown that it is possible to simulate the formation of fronts by a time integration of a baroclinic model without considering the effects of condensation. In order to verify his conclusion, the maps of surface

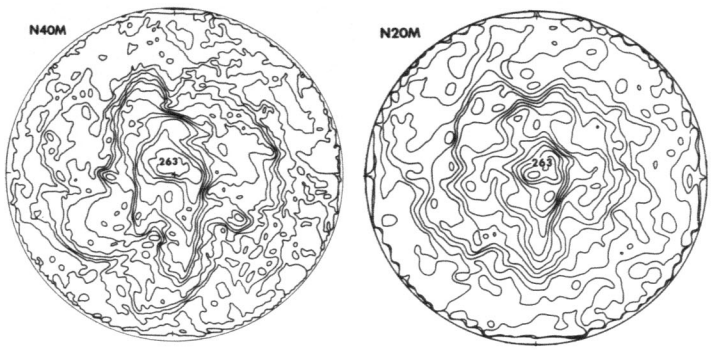

FIGURE 17.—Map of temperature at the lowest level (991 mb) on model day 173. Contour interval is 3°K.

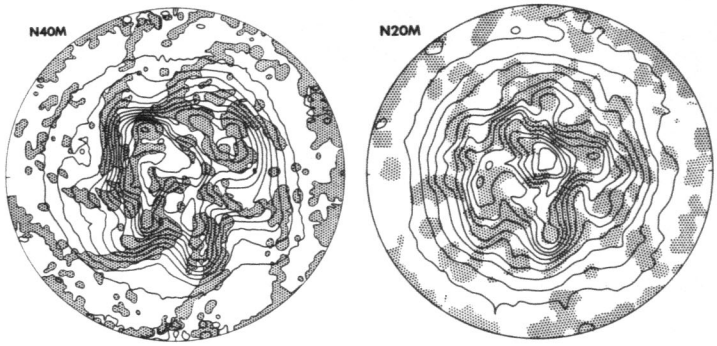

FIGURE 18.—Stereographic map of geopotential height of the 500-mb level on model day 173. Contour interval is 60 m. Shading indicates area of precipitation in excess of 0.1 cm day^{-1}; circular boundary, Equator.

pressure, temperature at level 9, and geopotential height of the 500-mb level on day 58.6 of the integration of the dry *N40D* model are made and are shown in figures 23 and 24. (See appendix II for a brief description of the *N40D* model.) These maps clearly show that the dry general circulation model is capable of producing frontlike systems.

Comparing the structure of the frontal system in the *N40M* atmosphere and in the *N40D* atmosphere, (see figs. 16, 17, 18, 23, and 24) we find the following differences:

1) The scale of cyclones associated with fronts at the earth's surface in the dry *N40D* atmosphere is generally larger than in the moist *N40M* atmosphere.

2) The widths of fronts in the former are significantly wider than in the latter.

3) The fronts in the *N40M* atmosphere extend toward lower latitudes than in the *N40D* atmosphere.

Such a scale reduction in the presence of condensation was suggested by Smagorinsky (1957) particularly by a reduction in the area of upward motion and an increase in the area of downward motion. In study M, it was demonstrated that the heat of condensation indeed produced the narrow area of intense convergence and reduced the scale of cyclones in the lower troposphere. This characteristic was also discussed in connection with prediction experiments (Smagorinsky and Staff Members 1967). In the dry *N40D* model, the scale of predominant cyclones near the earth's surface is similar to that at the 500-mb level, and the distribution of surface pressure is highly unrealistic; whereas in the moist *N40M* model, the cyclones with smaller scale develop near the earth's surface. These results reflect the dynamical consequence of the reduced static stability due to water phase changes, that is, a smaller scale of maximum baroclinic instability. The reduction of the area of convergence caused by the condensation process is probably responsible for the narrowness of the width of fronts in the moist model atmosphere.

The results shown in this section indicate that it is necessary to take into consideration the effect of the heat of condensation for a successful simulation of fronts and associated cyclone families. Each of the small cyclones has a controlling effect on local weather. Since these cyclones are not always resolved sufficiently by the *N40* grid, a further reduction in grid size is desirable for the successful forecast of local weather.

Recently, a numerical weather prediction model with very high horizontal resolution has been developed by Bushby and collaborators (Bushby and Timpson 1967). They obtain partially successful results in predicting frontal rain.

6. BUDGET OF EDDY KINETIC ENERGY

The major difference between the *N40M* and *N20M* atmospheres lies in the spatial distribution, particularly in the spectral distribution, of eddy kinetic energy. In this section, we shall briefly describe how the eddy kinetic energy is maintained in the *N40M* atmosphere. We shall discuss why the kinetic energy spectrum of the *N40M* atmosphere is different from that of the *N20M* atmosphere based upon an analysis of the energy budget in wave number space. An extensive study of the budget of eddy kinetic energy in the various parts of the model atmosphere will also be described in terms of wave number space.

A. SOURCES AND SINKS OF EDDY KINETIC ENERGY

Outside the tropical region, the distribution of sources and sinks of eddy kinetic energy in the *N40M* model atmosphere is very similar to that in the *N20D* atmosphere which was extensively described in study S. Therefore, we shall cover this subject only very briefly here.

Subtracting the prognostic equation of zonal kinetic energy from the equation of total kinetic energy, one gets the following equation describing the rate of change of eddy kinetic energy:

$$\frac{\partial \overline{K_E}^{\lambda}}{\partial t} = -\left[\frac{1}{a\cos\theta}\frac{\partial}{\partial\theta}(\cos\theta \cdot \overline{vK_E}^{\lambda}) + \frac{\partial}{\partial P}\overline{(\omega K_E)}^{\lambda}\right] + \langle K_Z \cdot K_E\rangle - \overline{\mathbf{V}' \cdot \nabla\phi'}^{\lambda} + \overline{\mathbf{V}' \cdot \mathbf{F}'}^{\lambda} \quad (18)$$

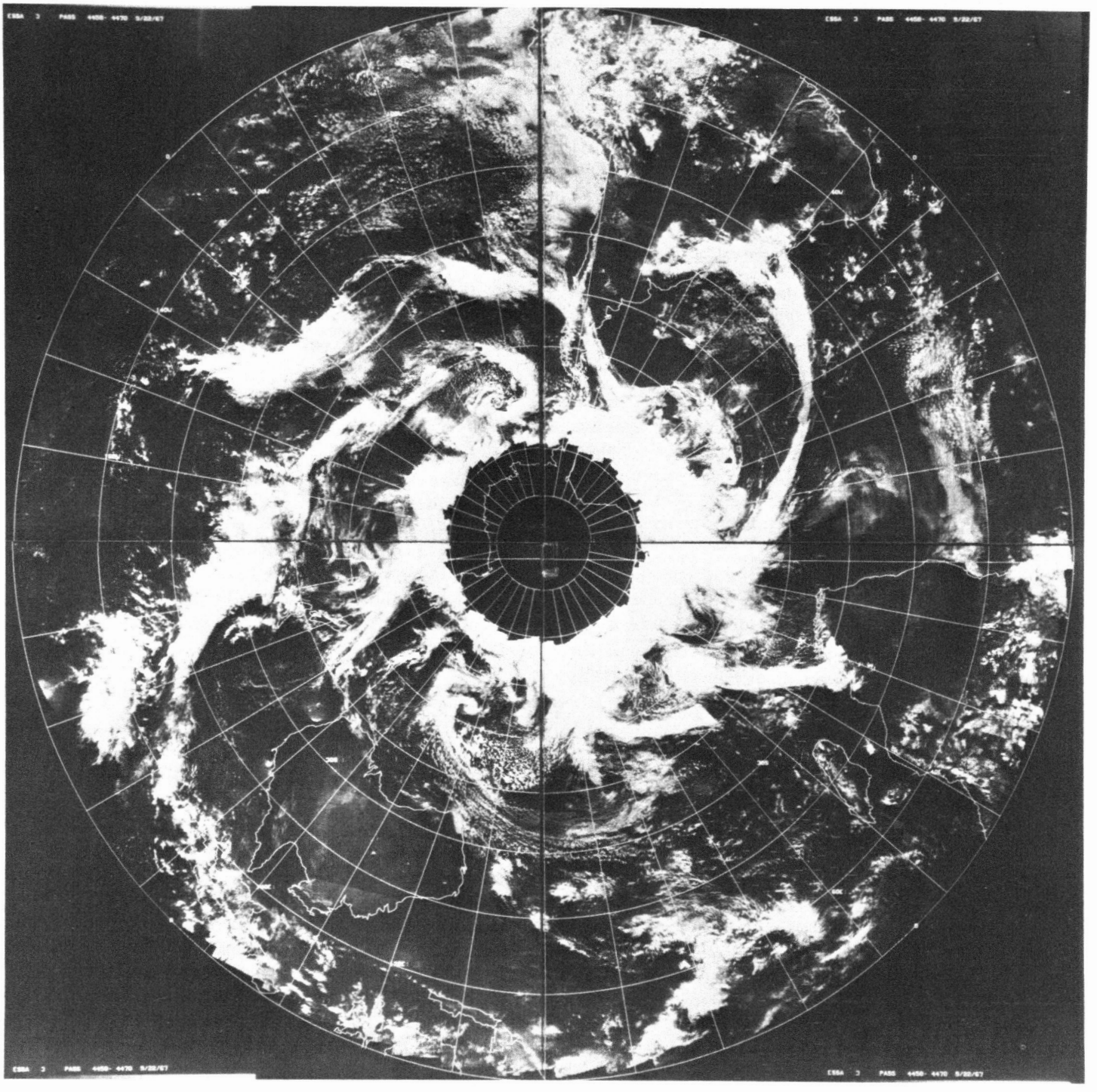

FIGURE 19.—Satellite, ESSA 3, photographic mosaic of the Southern Hemisphere on Sept. 22, 1967.

where

$$K_E \equiv K_T - K_Z$$

and

$$K_T = \tfrac{1}{2}\,(u^2+v^2)$$

and

$$K_Z = \tfrac{1}{2}\,((\overline{u}^{\lambda})^2+(\overline{v}^{\lambda})^2).$$

Also,

$$\langle K_Z \cdot K_E \rangle = \langle K_Z \cdot K_E \rangle_I + \langle K_Z \cdot K_E \rangle_{II}$$

where

$$\langle K_Z \cdot K_E \rangle_I = -\overline{u'v'}^{\lambda}\frac{1}{a}\frac{\partial \overline{u}^{\lambda}}{\partial \theta} - \overline{\omega' u'}^{\lambda}\frac{\partial \overline{u}^{\lambda}}{\partial P} - \frac{\tan\theta}{a}\overline{u}^{\lambda}\cdot\overline{u'v'}^{\lambda}$$

$$-\overline{v'^2}^{\lambda}\frac{1}{a}\frac{\partial \overline{v}^{\lambda}}{\partial \theta} - \overline{\omega' v'}^{\lambda}\frac{\partial \overline{v}^{\lambda}}{\partial P} + \frac{\tan\theta}{a}\overline{v}^{\lambda}\cdot\overline{u'^2}^{\lambda}$$

and

$$\langle K_Z \cdot K_E \rangle_{II} = \frac{1}{a\cos\theta}\frac{\partial}{\partial\theta}(\cos\theta \cdot \bar{u}^{\lambda} \cdot \overline{u'v'}^{\lambda}) + \frac{\partial}{\partial P}(\bar{u}^{\lambda} \cdot \overline{u'\omega'}^{\lambda}) + \frac{1}{a\cos\theta}\frac{\partial}{\partial\theta}(\cos\theta \cdot \bar{v}^{\lambda} \cdot \overline{v'^2}^{\lambda}) + \frac{\partial}{\partial P}(\bar{v}^{\lambda} \cdot \overline{v'\omega'}^{\lambda}).$$

In these equations, a, θ, λ, P, and t are the radius of the earth, latitude, longitude, pressure, and time, respectively. Here, u, v, and $\mathbf{V}$ are the northward and eastward components of the wind and the horizontal wind vector, respectively; ω is the vertical P-velocity and ϕ is the geopotential height of an isobaric surface. $\mathbf{F}$ is the frictional force due to vertical and horizontal subgrid scale mixing; $\overline{(\ )}^{\lambda}$ and $(\ )'$ indicate the zonal mean and the deviation from zonal mean, respectively.

In equation (18), the first term on the right-hand side of the equation represents the contribution of flux divergence, and the second term the contribution of energy exchange between zonal and eddy kinetic energy. The third term computes the rate of the production of eddy kinetic energy by the pressure gradient force, and the fourth term gives the rate of dissipation. The production term may be broken down into two parts, that is

$$-\overline{\mathbf{V}' \cdot \nabla\phi'}^{\lambda} = -\left[\nabla \cdot \overline{(\mathbf{V}'\phi')}^{\lambda} + \frac{\partial}{\partial P}\overline{(\omega'\phi')}^{\lambda}\right] - \overline{\omega'\alpha'}^{\lambda} \quad (19)$$

where α is specific volume. The first term on the right-hand side of this equation represents the energy exchange with the surroundings through the pressure interaction, and the second term represents the conversion of the eddy potential energy. Using equation (19), and taking a hemispheric average, one can convert equation (18), into

$$\frac{\overline{\partial \overline{K_E}^{\lambda}}^{H}}{\partial t} = -\frac{\partial}{\partial P}\overline{(\omega K_E)}^{\lambda H} + \overline{\langle K_Z \cdot K_E \rangle}^{H} - \frac{\partial}{\partial P}\overline{(\omega'\phi')}^{\lambda H} - \overline{\overline{\omega'\alpha'}^{\lambda}}^{H} + \overline{\overline{\mathbf{V}' \cdot \mathbf{F}'}^{\lambda}}^{H} \quad (20)$$

According to study S, the eddy conversion $(-\overline{\omega'\alpha'}^{\lambda})$ is at a maximum in the midtroposphere of the model atmosphere. The pressure interaction term $(-\overline{\omega'\phi'}^{\lambda})$ in turn transfers energy both upward and downward. The upward flux converges in the upper troposphere and is responsible for the eddy kinetic energy maximum there. On the other hand, the downward flux converges in the planetary boundary layer and compensates for the large dissipation there. The contribution of flux divergence of the eddy kinetic energy by the large-scale eddies, $\partial\overline{(\omega K_E)}^{\lambda}/\partial P$, is negligible.

Figures 25 through 27 show the latitude-height distributions of the eddy conversion, eddy pressure interaction, and eddy dissipation in the *N40M* atmosphere. (Figure 28 was found to be in error and was deleted in press.) Figures 25–27 indicate that the general features of the distributions of energy budget terms in the *N40M* atmosphere are similar to those of the *N20D* atmosphere, which we discussed in study S. There are, however, some important differences. In the dry *N20D* model, an area of large eddy conversion lies in middle latitudes, whereas in the *N40M* atmosphere, centers of large conversions are located in the Tropics as well. As pointed out in study M2, the tropical maximum of eddy conversion is produced by the generation of eddy potential energy from released heat of condensation. The cyclone in the model Tropics has a cold core near the earth's surface and a warm core in the upper troposphere. The level of maximum eddy conversion in the Tropics coincides with that of the warm core located around the 300-mb level. This is somewhat higher than the level of the maximum in middle latitudes. The upward flux of energy by the pressure interaction in the Tropics converges mainly around the 200-mb level and is responsible for the eddy kinetic energy maximum there. Except for the differences in the height of the maximum, the qualitative features of the distribution of the conversion term and of the pressure interaction term in the Tropics are very similar to those in middle latitudes. The major mechanism for the generation of eddy available potential energy in the Tropics, however, is different from that in middle latitudes. In a study of the Tropics of the *N20M* atmosphere, Manabe and Smagorinsky (M2) found that the flow of energy that predominates in the model Tropics is as follows: heat of condensation→eddy available potential energy→eddy kinetic energy→dissipation. In middle latitudes, it is well known, however, that the following process plays a major role: meridional heating contrast→zonal available potential energy→eddy available potential energy→eddy kinetic energy→dissipation. For further details of the energetics of a cyclone in the model Tropics, refer to the study M2.

B. SPECTRAL DISTRIBUTION OF THE BUDGET OF EDDY KINETIC ENERGY

Hemispheric spectrum—In this subsection, we shall discuss how the spectrum of eddy kinetic energy, which is described in subsection 4D, is maintained in the model atmosphere, and why the spectra of the *N40M* atmosphere are more realistic than those of the *N20M* atmosphere.

Assuming the hydrostatic relationship, and adopting pressure as a vertical coordinate, we may write the equation of motion in the spherical coordinate system as follows:

$$\partial\mathbf{V}/\partial t = -\mathcal{D}_3(\mathbf{V}) - \sin\theta\cdot(\dot{\lambda}+2\Omega)(\mathbf{k}\times\mathbf{V}) - \nabla\phi + \mathbf{F} \quad (21)$$

where

$$\mathcal{D}_3(\ ) = \frac{\partial}{a\partial\lambda}(u\cdot(\ )) + \frac{\partial}{a\cos\theta\partial\theta}(\cos\theta\cdot v(\ )) + \frac{\partial}{\partial P}(\omega\cdot(\ )).$$

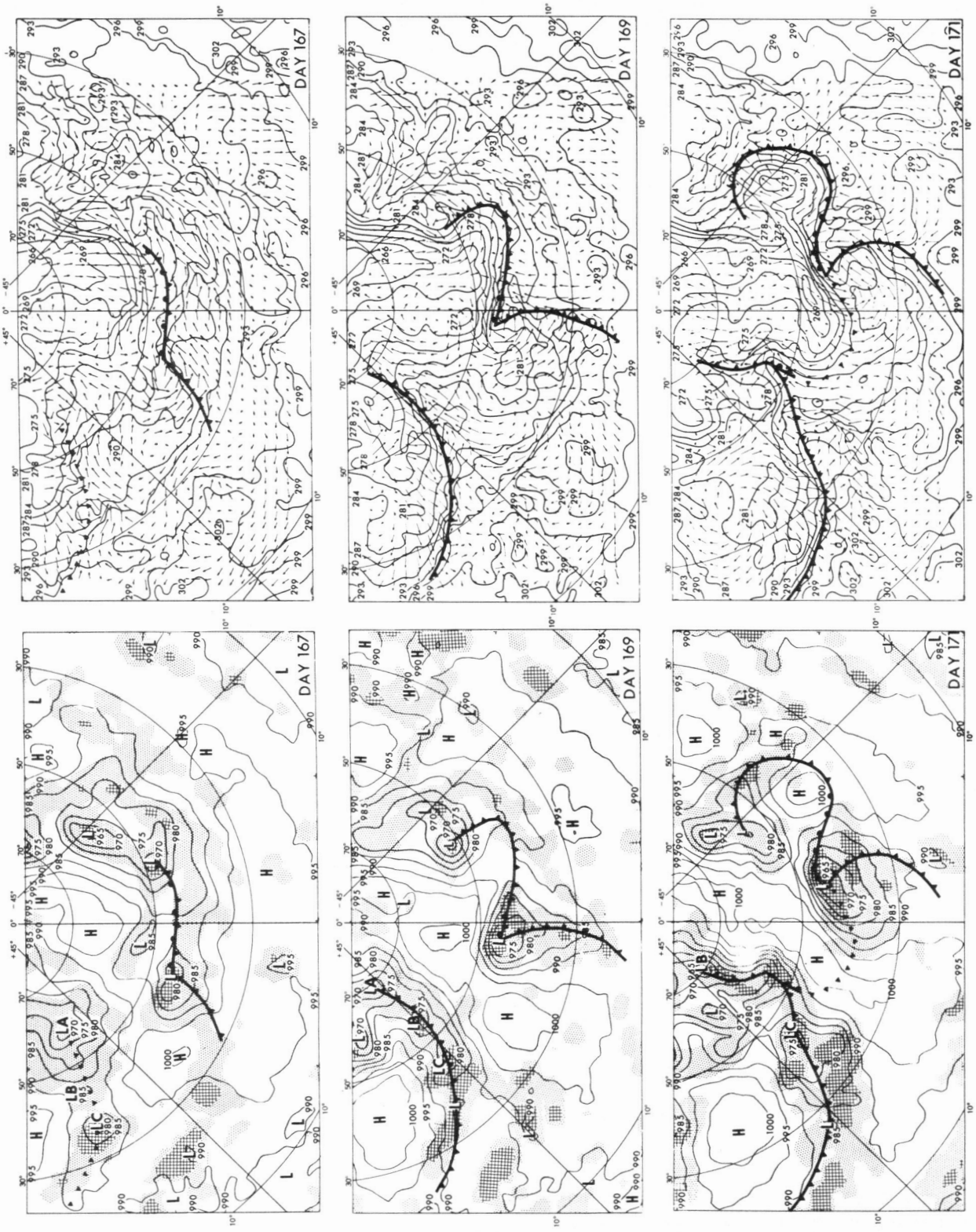

FIGURE 20.—Maps for model days 167, 169, and 171. Left side, surface-pressure map of the *N40M* atmosphere with a contour interval of 5 mb. The light shaded areas represent 24-hr precipitation exceeding 0.1 cm per day and heavy shading 1.0 cm per day. Fronts are indicated in the conventional way. Right side, wind and temperature fields at level 9 ($P/P^*=0.991$) of the *N40M* atmosphere. Temperatures are labeled in °K with a 3° contour interval. The length of the wind vector is proportional to wind speed.

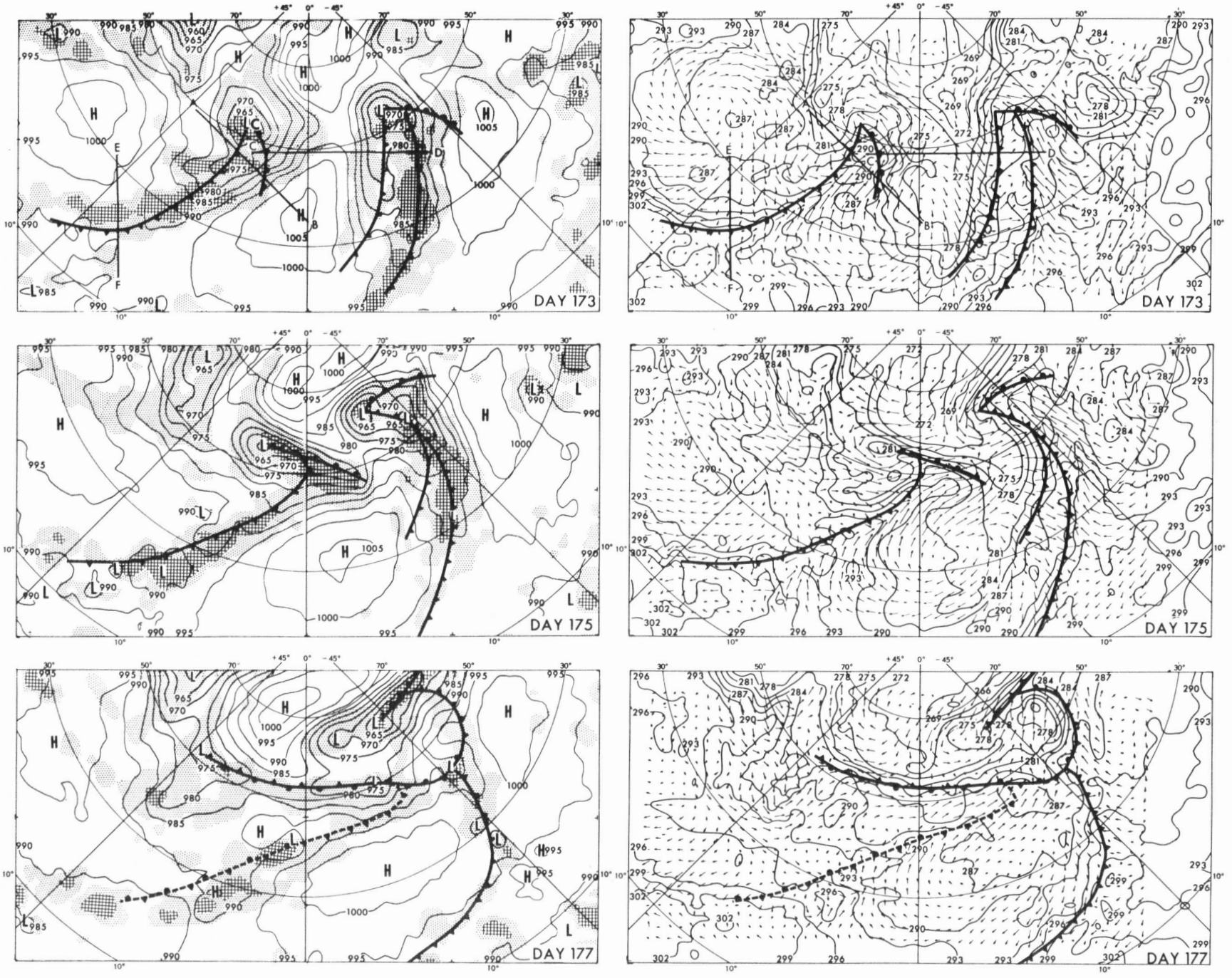

FIGURE 21.—Same as figure 20, but for model days 173, 175, and 177.

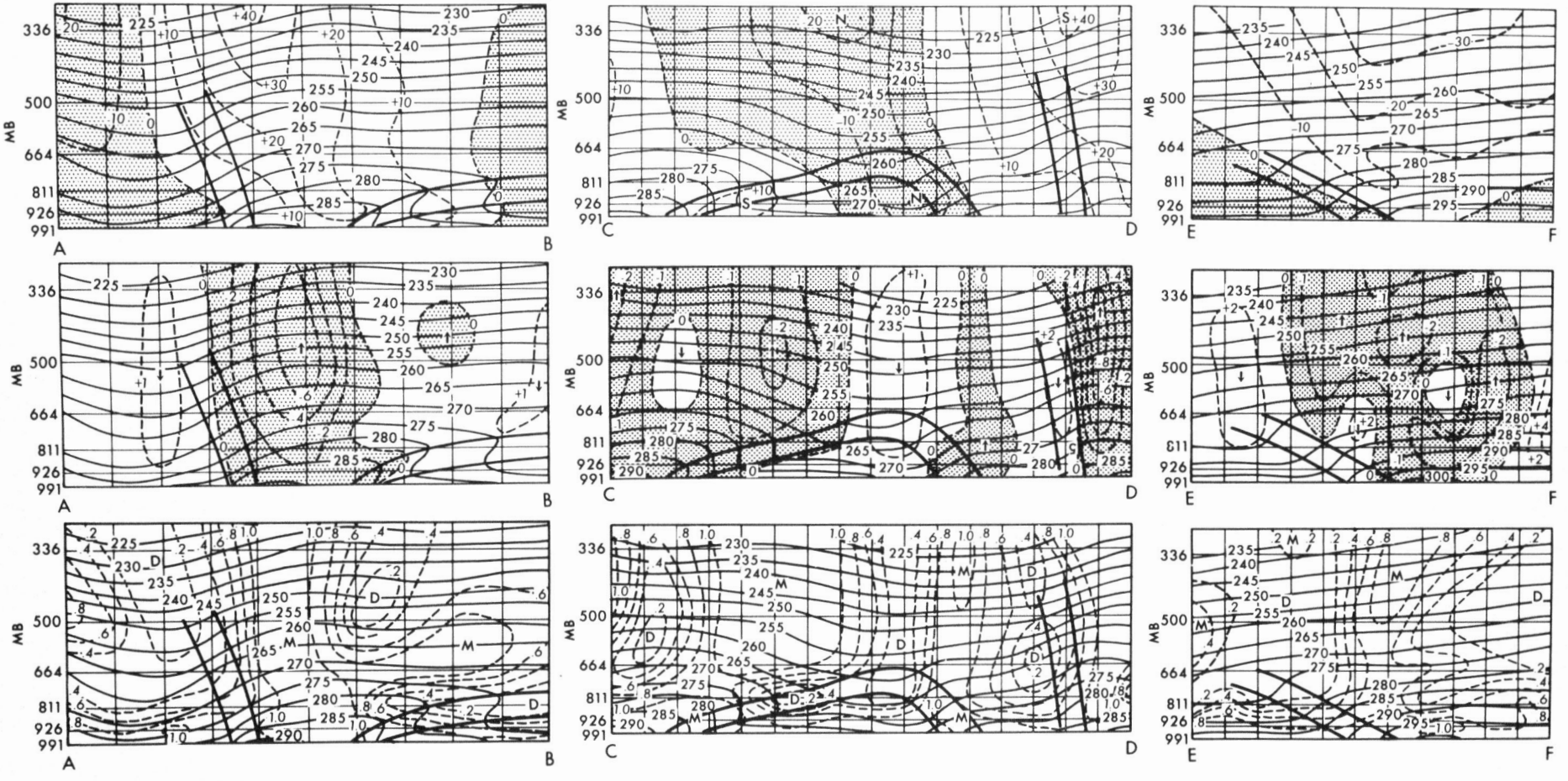

FIGURE 22.—Cross sections of the model fronts along the heavy lines marked A–B, C–D, and E–F, on model day 173 (fig. 21). The fronts are indicated by solid heavy lines, and temperature (°K) by solid light lines. Locations of grid points are indicated by vertical straight lines. The top row of cross sections shows the wind component normal to the cross sections (m sec^{-1}) superimposed on the temperature field; shaded areas indicate wind out of the page. The middle row shows vertical motion (microbars sec^{-1}) superimposed on temperature; areas of upward motion are shaded. The bottom row shows relative humidity superimposed on temperature.

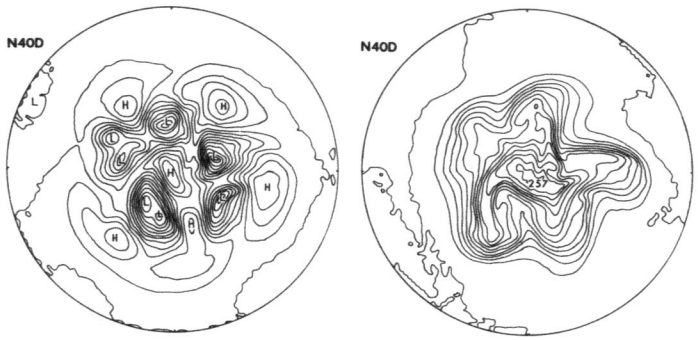

FIGURE 23.—Distribution of surface pressure (contour interval, 5 mb) and surface air temperature at the lowest level of 991 mb (contour interval, 3°K) on day 8.5 of the time integration of the *N40D* model are shown on the left- and right-hand side, respectively. The circular boundary indicates the Equator.

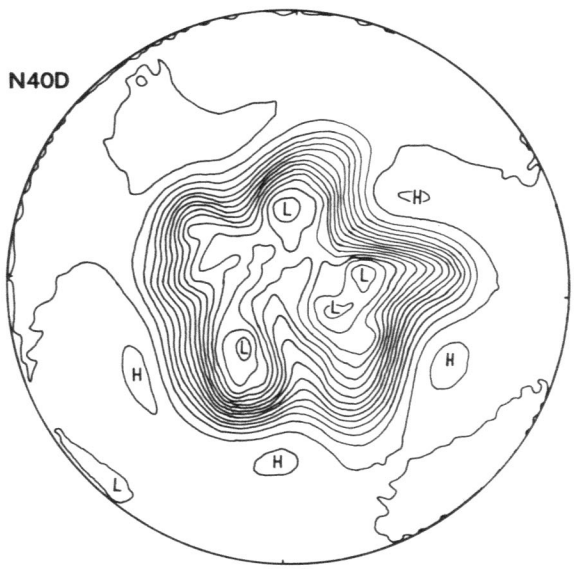

FIGURE 24.—Stereographic map of the geopotential height of the 500-mb level on day 8.5 of the time integration of the *N40D* model. The contour interval is 60 m. The circular boundary indicates the Equator.

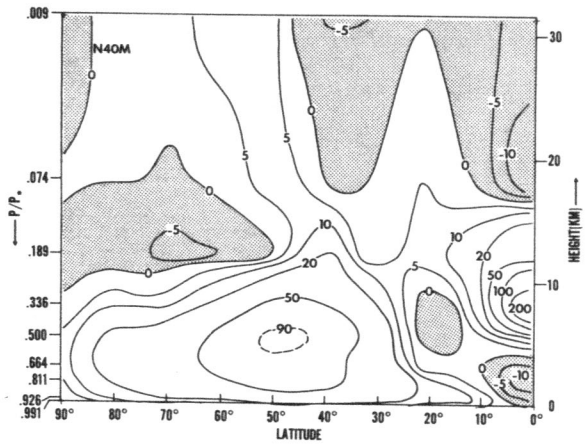

FIGURE 25.—Latitude-height distribution of the rate of the conversion of eddy potential energy ($-\overline{\omega'\alpha'}^{\lambda}$) in the *N40M* atmosphere. Units, 10^{-3} joules cm^{-2} mb^{-1} day^{-1}.

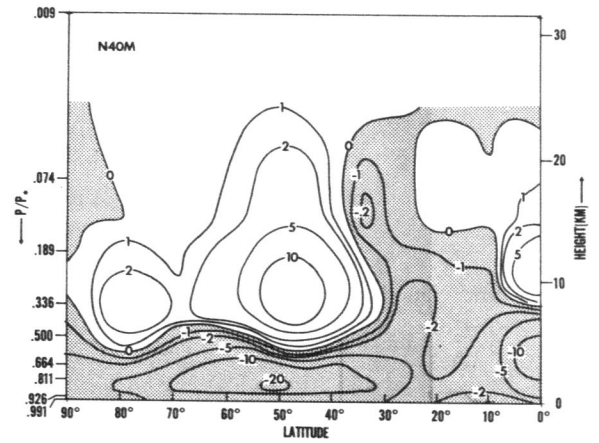

FIGURE 26.—Latitude-height distribution of the pressure interaction term ($-\overline{\omega'\phi'}^{\lambda}$) in the *N40M* atmosphere. The region of the downward flux of energy is shaded. Units, joules cm^{-2} day^{-1}.

Here, $\mathbf{k}$ is the unit vector pointing upward, and Ω is the angular velocity of the earth. For further details of the notation, see the explanation of equation (18). Analyzing each term of this equation into a Fourier series along latitude circles, we get

$$\left(\frac{\partial \mathbf{V}}{\partial t}\right)_n = -(\mathcal{D}_3(\mathbf{V}))_n - (\sin\theta\cdot(\dot{\lambda}+2\Omega)\cdot(\mathbf{k}\times\mathbf{V}))_n - (\nabla\phi)_n + (\mathbf{F})_n \tag{22}$$

where $(\ )_n$ denotes the Fourier components with wave number n. For example, if one expresses a function $f(x)$ in terms of its Fourier components,

$$f(x)=\sum_{n=0}^{N}(f(x))_n=\frac{1}{\sqrt{2\pi}}a_0+\sum_{n=1}^{N-1}\left(a_n\frac{\cos nx}{\sqrt{\pi}}+b_n\frac{\sin nx}{\sqrt{\pi}}\right)+a_N\frac{\cos Nx}{\sqrt{\pi}},$$

$$(f(x))_n=\left(a_n\frac{\cos nx}{\sqrt{\pi}}+b_n\frac{\sin nx}{\sqrt{\pi}}\right),\quad 0\le n\le N-1,$$

and

$$(f(x))_N=a_N\frac{\cos Nx}{\sqrt{\pi}}.$$

Multiplying each term on both sides of equation (22) by $(\mathbf{V})_n$ and applying the zonal mean operator, we obtain

$$\frac{\partial E(n)}{\partial t}=T(n)+P(n)-D(n) \tag{23}$$

where

$$E(n)=\tfrac{1}{2}\overline{(\mathbf{V})_n^2}^{\lambda},$$

$$T(n)=-\overline{(\mathbf{V})_n\cdot(\mathcal{D}_3(\mathbf{V}))_n}^{\lambda},$$

$$P(n)=-\overline{(\mathbf{V})_n\cdot(\nabla\phi)_n}^{\lambda},$$

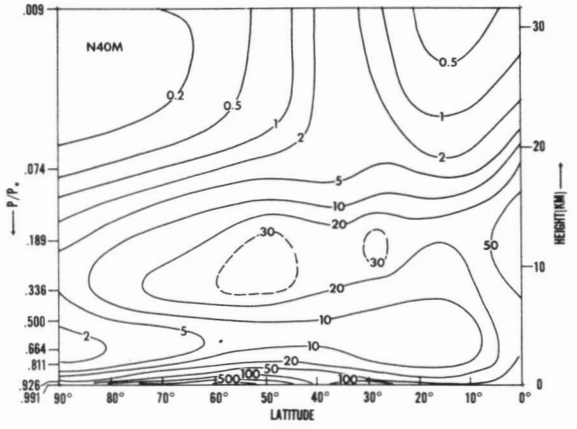

FIGURE 27.—Latitude-height distribution of the rate of eddy dissipation ($-\overline{\mathbf{V}'\cdot\mathbf{F}'}^{\lambda}$) in the *N40M* atmosphere. Units, 10^{-3} joules cm^{-2} mb^{-1} day^{-1}.

and

$$D(n)=-\overline{(\mathbf{V})_n\cdot(\mathbf{F})_n}^{\lambda}.$$

$E(n)$ denotes the kinetic energy of eddies with longitudinal wave number n; $T(n)$, $P(n)$, and $D(n)$ are the nonlinear inertia term, the production term, and dissipation term, respectively. These terms are computed along each latitude circle. The values of $\mathbf{V}$, $\mathcal{D}_3(\mathbf{V})$, $\nabla\phi$, and $\mathbf{F}$ at each latitude circle are obtained by interpolating between the grid points on the stereographic map. The Fourier coefficients are then obtained. Because of this interpolation, the sum of the contributions from all wave numbers is not necessarily correct. For example, $\overline{\sum_{n=1}^{N}T(n)}^{H}$ should be equal to the magnitude of the energy transfer from the zonal to the eddy kinetic energy. However, the former turned out to be significantly larger than the latter in the moist model atmospheres due to the interpolation. Since we are analyzing the period of quasi-equilibrium, the following approximate relation should hold:

$$\overline{T(n)}^{t}+\overline{P(n)}^{t}-\overline{D(n)}^{t}\approx 0.$$

In our analysis, this is not necessarily satisfied.

In figure 29, the hemispheric mean values of these terms are shown as a function of longitudinal wave number. The distributions for the *N40M* model and for the *N20M* model are given in the upper and lower parts of the figure. In the *N40M* atmosphere, there are significant differences between the production $\overline{P(n)}^{H}$ and the dissipation $\overline{D(n)}^{H}$, particularly in the wave number range of 4 to 8, where baroclinic instability prevails, and the nonlinear term $\overline{T(n)}^{H}$ plays a significant role in compensating for this imbalance. On the other hand, the difference between the production and the dissipation is very small in the *N20M* low resolution model, and the nonlinear term does little in redistributing energy from one wave number to others. (The net transfer of energy toward higher wave number components at wave number n can be estimated by the following integration with respect to wave number k:

$$S(n)=-\int_0^n \overline{T(k)}^{H}dk=\int_n^{\infty}\overline{T(k)}^{H}dk$$

since $S(\infty)=0$.)

Further examination of the nonlinear effect in the *N40M* atmosphere reveals that there is very little net transfer of energy from medium wave numbers to higher wave numbers. Instead, most of the energy, which is converted by baroclinic instability in the medium wave number range, is transferred to the low wave number range. Although the rate of change of the zonal kinetic energy is not shown in this figure, it is evident that the rate of energy transfer to zonal kinetic energy is significantly large as demonstrated later by the energy box diagram of figure 59. According to Starr (1953), this net transfer of energy from synoptic scale eddies to the zonal current is the main agent for maintaining the existing level of zonal kinetic energy in the actual atmosphere. Such a net transfer is missing in the *N20M* atmosphere.

In recent discussions of two-dimensional turbulence, Kraichnan (1967) and Leith (1968) noted that two kinds of inertial ranges could formally be defined, that is, that of Kolmogoroff in which energy is transferred through wave number space, and a new one in which mean square vorticity, but not energy, is transferred. The first leads to the familiar minus 5/3 power law. Kraichnan predicts the development of a minus 5/3 power range at wave numbers lower than those of the energy source and the development of a minus 3 power range at wave numbers higher than those of energy sources. In the former, kinetic energy is transferred to large scale, whereas in the latter, no kinetic energy is transferred toward small scales. The recent results from a numerical time integration of the barotropic vorticity equation by Lilly (1968) seem to substantiate the theory of Kraichnan and Leith.

Figure 30 shows the spectrum of eddy kinetic energy in the latitude belt ranging from 15° to 81° of the *N40M* model. In the high-frequency parts of the spectrum, the slope of the plotting indicates approximately minus 3 power which is not substantially different from Kraichnan's. This result is not inconsistent with the smallness of the energy cascade in the high-frequency range. It is interesting that such a slope emerges despite the depletion of kinetic energy by the nonlinear viscosity in the model atmosphere. The spectral distribution of the eddy kinetic energy of the geostrophic wind in the actual atmosphere, which was computed by Wiin-Nielsen (1967), is plotted for the sake of comparison. His spectrum also indicates a slope of approximately minus 3 power for the range of wave numbers larger than 8.

Dissipation spectra—In order to examine the difference between the *N40M* model and the *N20M* model further, we shall compare in detail the spectrum of kinetic energy dissipation in the two moist model atmospheres. In figure 31 are shown the rates of the dissipation at various wave numbers by horizontal and vertical mixing. This figure clearly indicates that the horizontal dissipation of kinetic energy takes place not only at large but also at

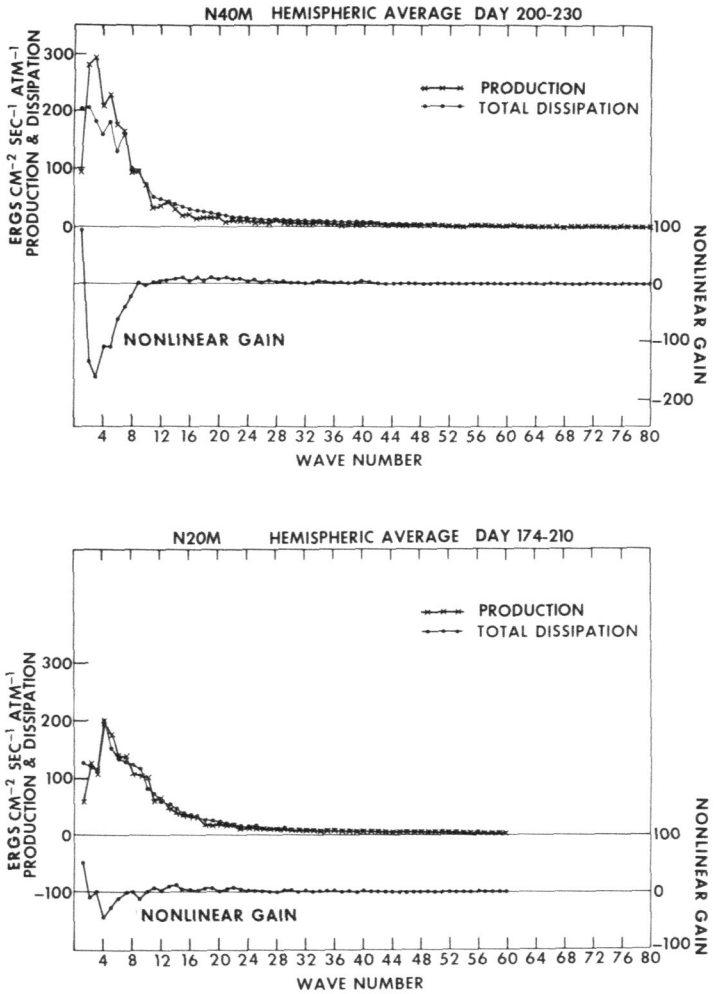

FIGURE 29.—Spectral distribution of the hemispheric mean values of the nonlinear term $T(n)$, production term $P(n)$, and dissipation term $-D(n)$. Note that the zero line of $T(n)$ is different from the zero lines for the other terms.

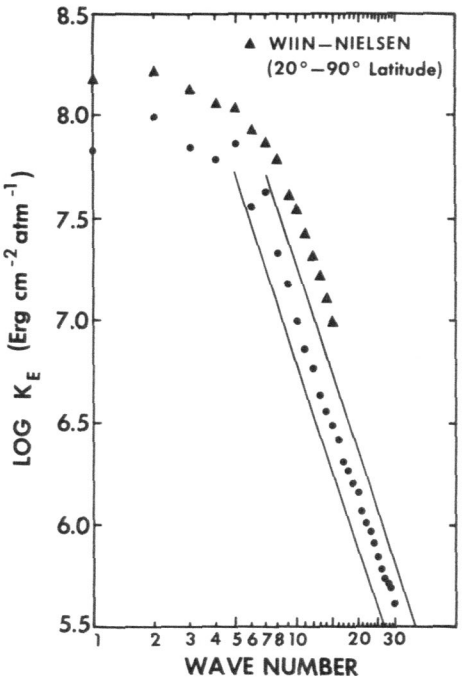

FIGURE 30.—Spectral distribution of the vertical integral of eddy kinetic energy of the *N40M* model (latitude 15°–81°). The slanted lines have a −3.0 slope. The observed spectrum by Wiin-Nielsen (1967) is also shown.

small longitudinal wave numbers. In other words, the rate of horizontal dissipation is significantly large at the wave numbers of baroclinic instability or at the wave numbers where energy is mainly transferred from high to low longitudinal wave numbers. This figure also reveals that the relative magnitude of dissipation by horizontal mixing and by vertical mixing depends upon the resolution of the model. Although the partitioning differs, the total dissipation does not, being mainly controlled by the energy made available through generation. In the *N20M* atmosphere, the rate of vertical dissipation is much less than the rate of horizontal dissipation; whereas in the *N40M* model, both rates have comparable magnitudes. In *N20M*, the eddy kinetic energy of medium wave numbers is dissipated mainly in situ by horizontal mixing; whereas in *N40M* it is transferred to lower longitudinal wave numbers where it is dissipated by both vertical and horizontal mixing.

The significant decrease of horizontal dissipation accompanying the increase in the resolution of the horizontal grid indicates that the effective viscosity acting on the synoptic scale disturbances decreases with increasing resolution. Since the scale at which the nonlinear dissipation is very effective decreases with decreasing grid size, it is reasonable that dissipation of large-scale motion by horizontal mixing is larger for the low resolution model than for the high resolution model. This is the major reason why the *N40M* atmosphere has larger eddy kinetic energy, larger decascade of energy from medium wave numbers to low wave numbers, and more dissipation by vertical mixing than the *N20M* atmosphere. It is expected that further increase of horizontal resolution should result in a more realistic atmosphere, because of the greater separation between the synoptic scale and the scale of dissipation by horizontal subgrid scale mixing.

Spectra of kinetic energy production ($-\overline{\mathbf{V}\cdot\nabla\phi}^{H}$). Another important factor controlling the spectrum of eddy kinetic energy is the production of eddy kinetic energy resulting from the conversion of potential energy.[2] In figure 32, the spectra of kinetic energy production of both models are shown. This figure indicates that magnitude of the production in the *N40M* atmosphere is significantly larger than in the *N20M* atmosphere in the range of wave numbers less than 8. The increase of kinetic energy production at lower wave numbers resulting from the improvement in the horizontal resolution seems to be one of the major reasons why the kinetic energy of the long waves in the *N40M* atmosphere is much larger than in the *N20M* atmosphere.

It is rather surprising, however, that the maximum difference between the production spectra of the two

[2] Note that the hemispheric mean spectrum of the production term is identical with that of conversion. In practice, there is some difference mainly because of the error caused by interpolation and finite differencing.

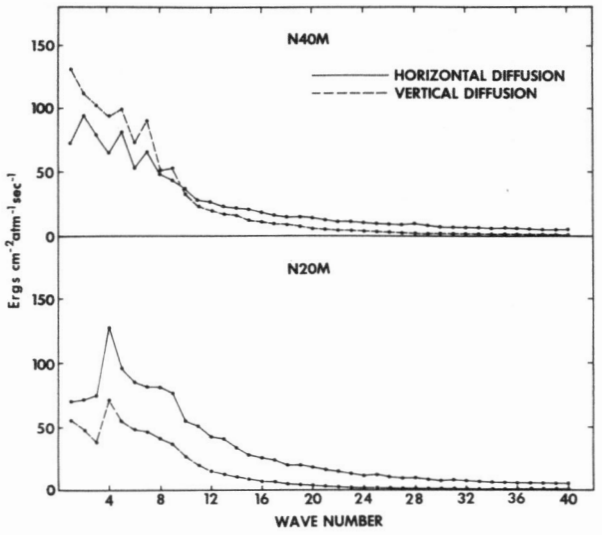

FIGURE 31.—Hemispheric mean rates of dissipation by subgrid scale mixing as a function of wave number for the two models. Solid and dashed lines indicate the dissipation by horizontal and vertical mixing, respectively.

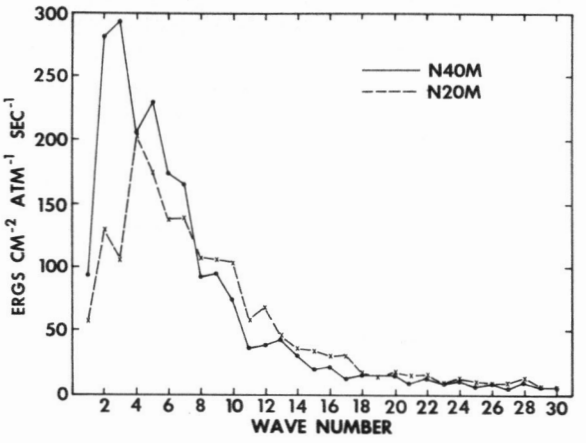

FIGURE 32.—Spectral distribution (hemispheric average) of the rate of change of eddy kinetic energy by the production term $P(n)$.

models appears at wave numbers 2 and 3. Since such a long wave can be represented by a relatively coarse grid, the doubling of the resolution should hardly improve the accuracy of representation. Therefore, the improvement of the finite-difference representation may not be the direct cause for this difference in the production spectrum. As we have pointed out, horizontal dissipation accounts for most of the dissipation in the *N20M* atmosphere; whereas in the *N40M* atmosphere, the contribution of vertical dissipation is increased and the contribution of horizontal dissipation is decreased. It is probable that the differences in the magnitude and in the vertical distribution of dissipation between the two model atmospheres cause the differences in amplitudes and in the structure of the long waves and accordingly cause the differences in the spectra of production and kinetic energy at small wave numbers.

Spectra in middle and low latitudes—So far, we have discussed the hemispheric mean spectrum of various components of the kinetic energy budget. As previously mentioned, the energetics of middle latitudes are somewhat different from the energetics of the Tropics. Therefore, it is worthwhile to examine the kinetic energy budget for middle latitudes and the Tropics separately.

The spectra of the eddy kinetic energy in both the middle latitudes and the Tropics of the *N40M* model are shown in figure 33. In middle latitudes, the eddy kinetic energy of the meridional component of the wind is maximum in the range of wave numbers 4 to 8, whereas that of the zonal component of the wind generally increases with decreasing wave numbers. In the Tropics, the eddy kinetic energy of the zonal component of the wind is a maximum at low wave numbers ranging from 1 to 5 and is much larger than that of the meridional component due probably to the effect of the equatorial boundary. The relative magnitudes of the two, however, approach each other with increasing wave numbers. The spectral distribution of the energy balance components in middle latitudes and in the Tropics of the *N40M* model are shown in figure 34. In middle latitudes, the production term $P(n)$ is maximum in the range of wave numbers 5 to 7 where the eddy kinetic energy of the meridional wind is maximum. The eddy dissipation term $D(n)$ is maximum in the range of wave numbers 1 to 8. The magnitude of the production term exceeds the magnitude of the dissipation term in the wave number range of 4 to 10 and constitutes a net supply of eddy kinetic energy in this range. This excess of kinetic energy may be mainly transferred to lower wave numbers (less than 4) barotropically. Although it is not explicitly shown in this figure, a large amount of energy is also transferred to zonal kinetic energy by this process. This subject will be discussed again in section 8. There seems to be a small cascade of energy toward higher wave numbers.

In the Tropics, both the dissipation and production terms have significant magnitude up to very large wave numbers, suggesting the predominance of small-scale disturbances. As pointed out in study M2, the generation of eddy available potential energy from released heat of condensation is responsible for such disturbances with wave lengths of 2000 to 3000 km. It is also interesting that the largest production of kinetic energy takes place in the range of wave numbers 1 to 5 where the eddy kinetic energy is maximum. Since the magnitude of eddy kinetic energy is very small in the Tropics of the dry model, as the results of study M2 indicate, it is clear that the heat of condensation is responsible for the development of such long waves. It is not clear, however, why such long waves can develop in the Tropics of the moist models. Further study is necessary in order to establish the mechanism of the growth of the long waves. In the range of wave numbers 1 to 13, the production of kinetic energy is larger than dissipation. As was the case in middle latitudes, the excess energy may be mostly transferred to the zonal current, and the energy transfer toward higher wave numbers seems to be very small.

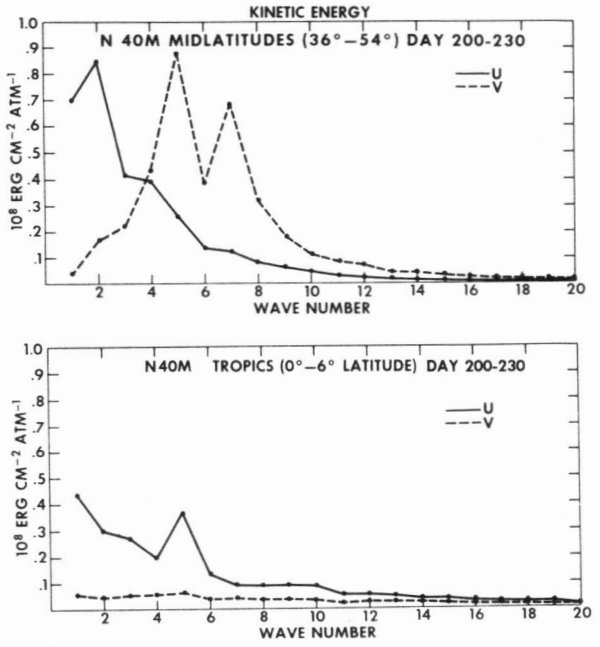

FIGURE 33.—Kinetic energy spectrum of the *N40M* model for middle latitudes and the Tropics.

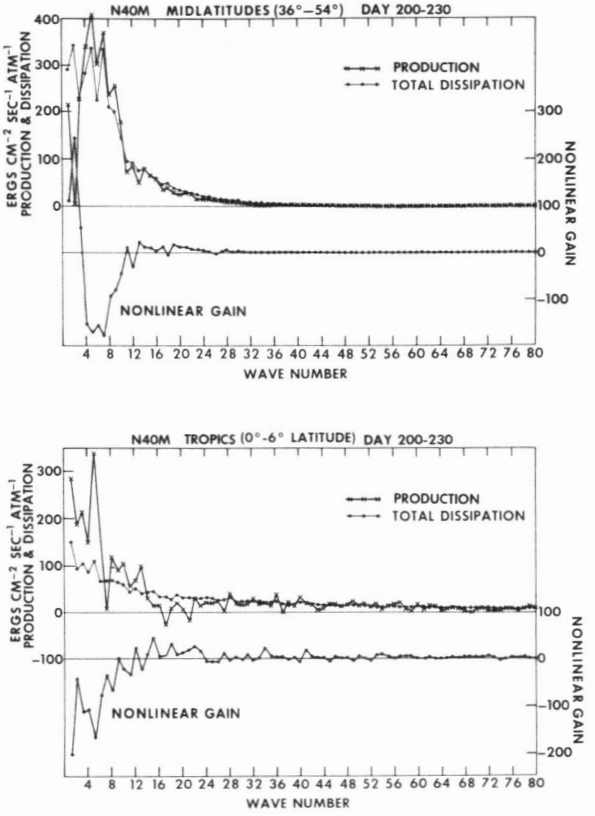

FIGURE 34.—Spectral distribution of the rate of change of eddy kinetic energy due to the nonlinear term, the production term, and the dissipation term. Upper half, middle latitudes (36° to 54° latitude); lower half, Tropics (0° to 6° latitude).

C. VERTICAL DISTRIBUTION OF THE ENERGY SPECTRUM

According to the comparison between the surface pressure map and the geopotential height map of the 500-mb level of the *N40M* atmosphere (figs. 16 and 18), the characteristic scale of waves at the 500-mb level is significantly larger than that of the disturbances near the earth's surface. Also, as figure 38 indicates, the characteristic wavelength in the model stratosphere is longer than in the model troposphere. These results indicate that the characteristic scale of disturbances of the moist atmosphere generally increases with altitude in the stratosphere as well as in the troposphere. In order to determine how the vertical distribution of the energy spectrum is maintained, we shall examine the vertical distribution of the various components of the energy balance in wave number space.

Applying the hemispheric mean operator and using the relation

$$-\overline{(\mathbf{V})_n \cdot (\nabla\phi)_n}^{\lambda} = -\nabla \cdot \overline{((\mathbf{V})_n(\phi)_n)}^{\lambda} - \frac{\partial}{\partial P}\overline{((\omega_n \cdot (\phi)_n)}^{\lambda} - \overline{(\omega)_n \cdot (\alpha)_n}^{\lambda}, \quad (24)$$

we can transform equation (22) to

$$\overline{(\mathbf{V})_n\left(\frac{\partial \mathbf{V}}{\partial t}\right)_n}^{\lambda H} = -\overline{(\mathbf{V})_n \cdot \left(\mathbf{V}\cdot\nabla\mathbf{V} + \omega\frac{\partial \mathbf{V}}{\partial P}\right)_n}^{\lambda H} - \frac{\partial}{\partial P}\overline{((\omega_n \cdot (\phi)_n)}^{\lambda H}\ \overline{(\omega)_n \cdot (\alpha)_n}^{\lambda H} + \overline{(\mathbf{V})_n \cdot (\mathbf{F})_n}^{\lambda H}.$$

The first term on the right-hand side of this equation represents the contribution of the nonlinear term to the change of the kinetic energy of the wind component with wave number n. The second and third terms represent the contributions of the pressure interaction and conversion terms, respectively, and the fourth term represents the contribution of dissipation. Figure 35 shows the spectral distributions of the conversion terms at various levels in the *N40M* atmosphere. These distributions represent the area averages of each term in the latitude belts ranging from 15° to 81° N. The tropical area is not included in this averaging because the vertical distribution of the energy budget in the Tropics is somewhat different in middle latitudes.

According to this figure, the characteristic scale of eddy conversion in the *N40M* atmosphere increases with increasing altitude throughout the troposphere. In the middle troposphere, the eddy conversion is a maximum around wave numbers 3 to 7; whereas in the upper troposphere it is maximum at wave number 2. Also, the eddy conversion at higher wave numbers ($n>10$) has significant magnitude in the lower troposphere partly due to condensation, whereas it does not in the upper troposphere. This increase of the characteristic scale of conversion with increasing altitude is consistent with the increase of the scale of the eddies with height.

Another factor that determines the change of kinetic energy is the pressure interaction; figure 36 shows the spectral distribution of this term. In the upper tropo-

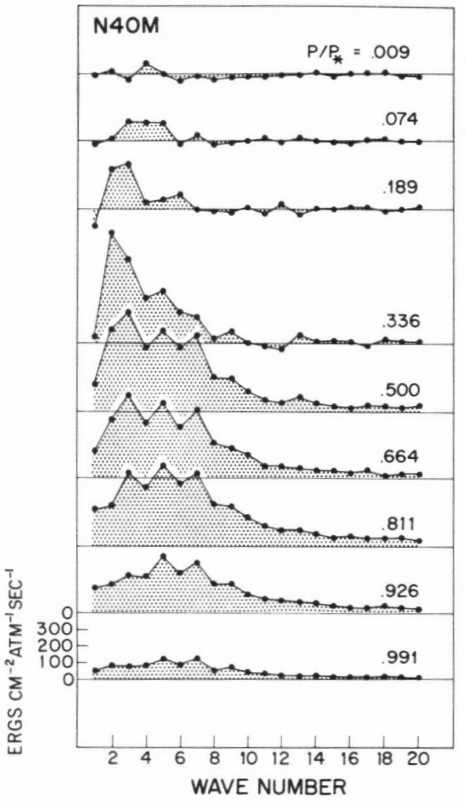

FIGURE 35.—Spectral distribution of the conversion term $(-\overline{(\omega)_n(\alpha)_n}^A)$ at various levels in the *N40M* atmosphere. Here, $\overline{(\quad)}^A$ indicates the average for the area between 15° to 81° latitude.

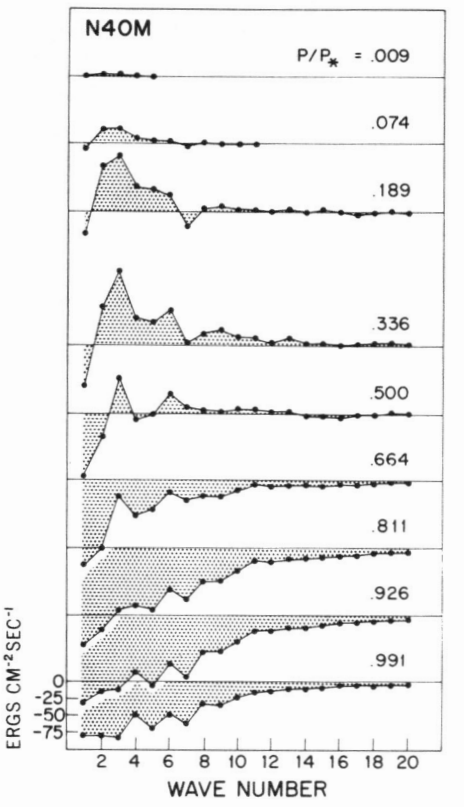

FIGURE 36.—Spectral distribution of the pressure interaction term $(-\overline{(\omega)_n(\phi)_n}^A)$ at various levels in the *N40M* atmosphere. Here, $\overline{(\quad)}^A$ indicates the average for the area between 15° to 81° latitude.

sphere, that is, above the 500-mb level, the pressure interaction transfers energy upward. On the other hand, it transfers energy downward at very small wave numbers below the 500-mb level. Accordingly, the convergence of energy takes place above the 300-mb level and below the the 800-mb level. In the intermediate layer, between the 300-mb and 800-mb levels, divergence of energy flux takes place. Above the 300-mb level, upward energy flux by the pressure interaction increases its scale with increasing altitude and helps maintain very long waves in the stratosphere. In the layer of energy divergence (the 300-mb to 800-mb layer), the characteristic scale of the pressure interaction is very large, and the energy of very long waves is depleted. In short, the pressure interaction contributes to the increase of the scale of eddies with increasing altitude above the 850-mb level.

Summing up the contributions of the pressure interaction and of the conversion, we obtain the net rate of the production of kinetic energy by the pressure gradient force. The vertical distribution of the spectrum of the rate of the net production is shown in figure 37. This figure shows that the baroclinic effect as a whole is responsible for the increase in the scale of eddies with increasing altitude above the planetary boundary layer. Figure 37 also indicates that the nonlinear transfer counterbalances this baroclinic effect. In general, the nonlinear transfer depletes the energy of medium wave numbers and mainly increases the energy of the zero wave number, that is, the zonal kinetic energy. In the free atmosphere the characteristic scale of depletion by the nonlinear transfer increases with increasing altitude.

In the planetary boundary layer or below the 850-mb level, the large convergence of downward energy flux at very low wave numbers contributes to the production of the energy of very long waves. According to figure 37, the energy of such long waves, however, is depleted very rapidly by the dissipation due to the vertical mixing and surface drag which predominate in the planetary boundary layers. The contribution of the dissipation due to the horizontal mixing is relatively small. Since the dissipation by surface drag is proportional to the cube of the wind speed and since the kinetic energy of the surface wind increases with decreasing wave number, the dissipation by vertical mixing and surface drag increases with decreasing wave number. Therefore, vertical mixing dissipates the kinetic energy of very long waves and counterbalances the production in the planetary boundary layer.

The basic cause for the increase of the scale of the disturbances with height in the troposphere of the moist

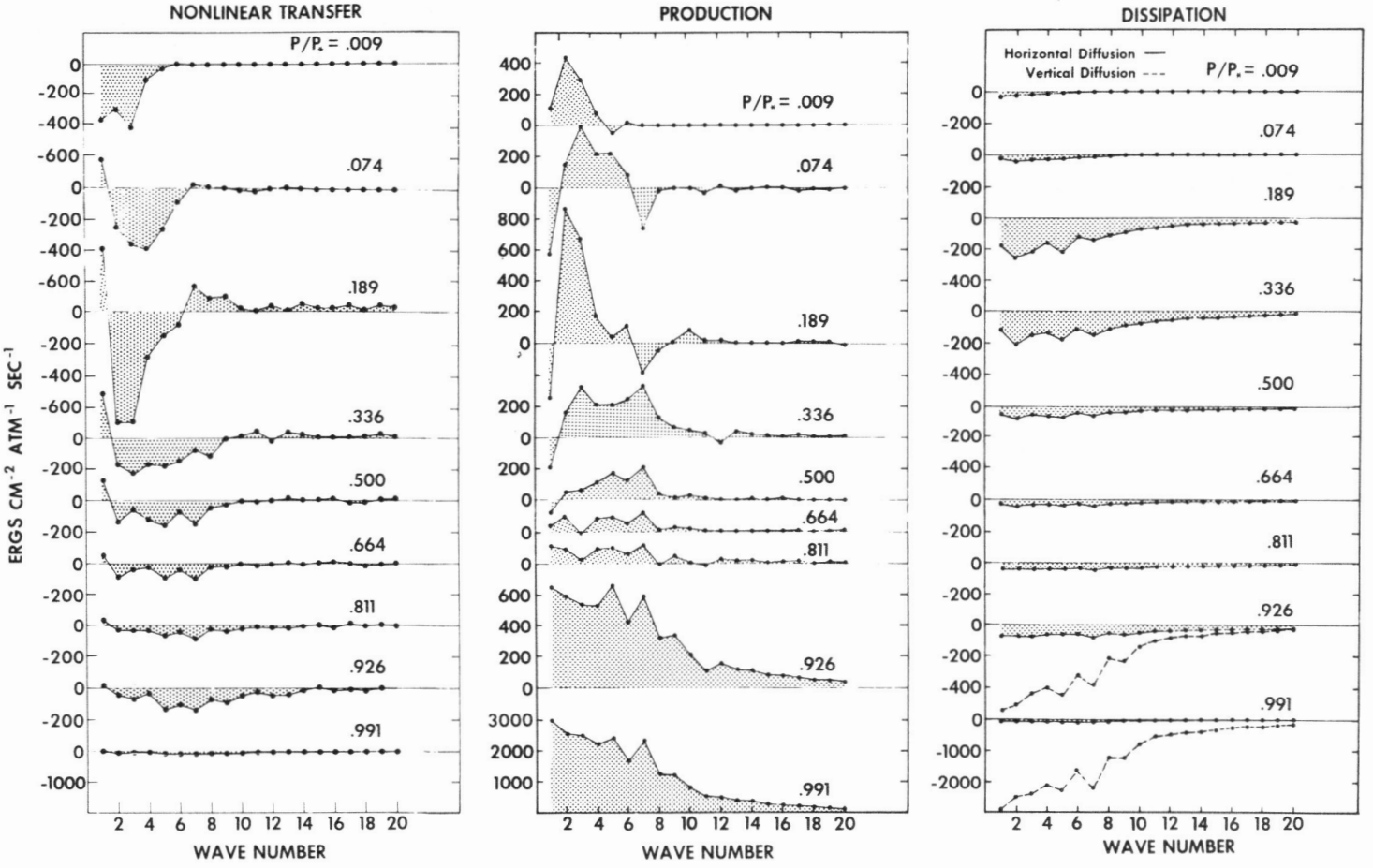

FIGURE 37.—Spectral distribution of the contribution of each term to the rate of change of eddy kinetic energy at various levels of the *N40M* atmosphere. The contribution of the nonlinear term $\overline{(-(\mathbf{V})_n\cdot(\mathbf{V}\cdot\nabla\mathbf{V}+\omega(\partial\mathbf{V}/\partial P))_n}^A$), the production term $\overline{(-(\mathbf{V})_n\cdot(\nabla\phi)_n}^A$), and the dissipation term $\overline{((\mathbf{V})_n\cdot(\mathbf{F})_n}^A$) are shown in the left, middle, and right diagrams, respectively. Here, $\overline{(\quad)}^A$ indicates the average for the area between 15° and 81° latitude.

model becomes evident if we compare the characteristic scale of disturbances of the moist atmosphere with that of the dry atmosphere. Figure 38 shows such a comparison. We note that the dependence of the effective wave number on height is hardly detectable in the *N40D* troposphere, whereas it is evident in the *N40M* troposphere. One can also identify the effect of condensation on the spectral distribution of the eddy conversion by comparing the conversion spectra of the *N40D* atmosphere shown in figure 39 with those of the *N40M* atmosphere shown in figure 35. In the *N40D* troposphere, the conversion spectra have a distinct maximum at wave number 5, whereas in the moist *N40M* troposphere, it spreads over a wider range of wave numbers. These results explain why intense large-scale cyclones dominate the map of surface pressure of the *N40D* atmosphere and less intense, smaller scale cyclones are evident in the corresponding map of the *N40M* model. Also, the comparison between figures 35 and 39 seems to show that the effects of condensation tend to develop ultralong waves particularly in the upper troposphere.

In order to compare the energetics of stratospheric and tropospheric motion, spectral distributions of various components of the kinetic energy budget for the model stratosphere and those for the whole model atmosphere are given in figure 40. In the model stratosphere (levels 1 and 2), eddy kinetic energy is mainly produced at wave numbers 2 and 3 by the pressure interactions. This eddy kinetic energy is transferred in turn to the kinetic energy of the zonal flow inertially by nonlinear transfer. On the other hand, the eddy kinetic energy of the troposphere is mainly fed by the conversion from eddy potential energy in the range of wave numbers between 2 and 8. A significant part of this eddy kinetic energy is transferred to zonal kinetic energy by the decascade. In summary, the zonal kinetic energy of the model stratosphere is maintained by the transfer of energy from very long waves; whereas in the troposphere the energy of the zonal current is acquired from the waves of medium wave numbers between 2 and 8. Similar results have been obtained by Teweles (1963) and Saltzman and Teweles (1964) for the actual atmosphere. They computed the energy exchange

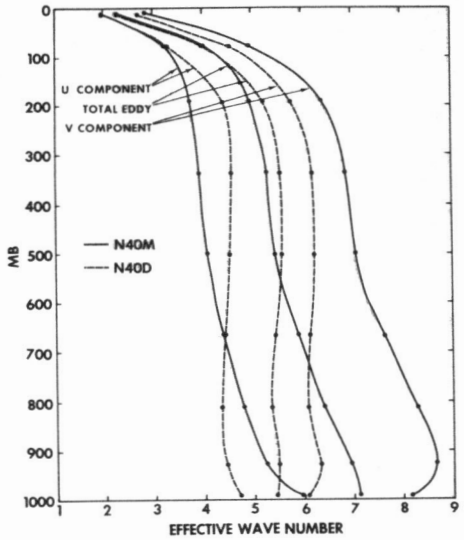

FIGURE 38.—Vertical distribution of the effective wave number in the *N40M* and *N40D* atmospheres are shown by solid and dashed lines, respectively. (See subsection 4D for the exact definition of the effective wave number $\bar{n}$.) In order to exclude the tropical eddies from the analysis, the effective wave number is computed for the area between 15° and 81° latitude.

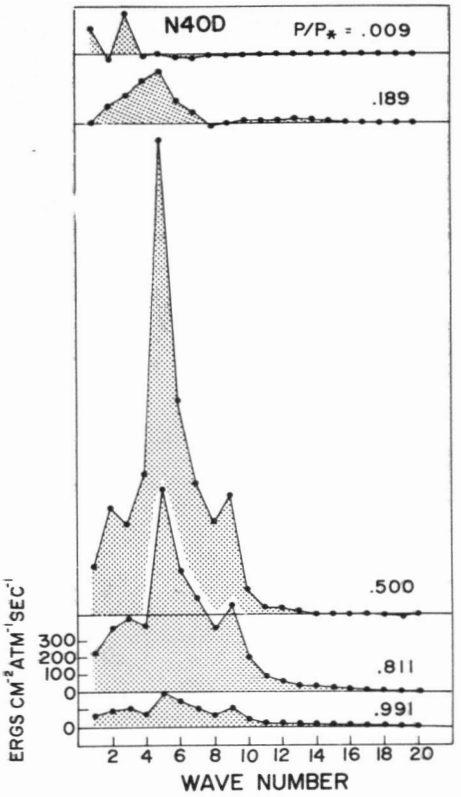

FIGURE 39.—Spectral distribution of the conversion term $(-\overline{(\omega)_n(\alpha)_n}^A)$ at various levels in the *N40D* atmosphere. Here, $\overline{(\quad)}^A$ indicates the average for the area between 15° and 81° latitude.

among the waves with different wave numbers by the barotropic processes and obtained results similar to those described here.

7. BUDGET OF ANGULAR MOMENTUM, HEAT, AND MOISTURE

Before discussing the budget of various quantities, it is desirable to define the transport of any quantity q by the large-scale eddies and the meridional circulation.

The poleward transport of q by large-scale eddies is given by the expression

$$(2\pi a \cos\theta/g)\int_0^{P_{MAX}} \overline{(v-\bar{v}^{\lambda})(q-\bar{q}^{\lambda})}^{\lambda} dP,$$

and the poleward transport of q by meridional circulation is given by the expression

$$(2\pi a \cos\theta/g)\int_0^{P_{MAX}} \bar{v}^{\lambda}\cdot\bar{q}^{\lambda}\, dP,$$

where P_{MAX} is maximum surface pressure and v is the meridional component of the wind.

A. ANGULAR MOMENTUM

Transport—The latitudinal distributions of the vertical integral of poleward transport of angular momentum by large-scale eddies, meridional circulation, and subgrid scale Reynolds stress in the *N40M* atmosphere are contrasted with those in the *N20M* atmosphere in figure 41. This figure shows that one of the important differences between the two models lies in the magnitude of the subgrid scale transport. In the low resolution *N20M* atmosphere, this "transport" is almost as large as the large-scale eddy transport in low latitudes. In the high resolution model (*N40M*), it has negligible magnitude indicating the drastic decrease in the effective Reynolds stress as a result of the doubling of the horizontal resolution. On the other hand, the magnitude of the poleward transport by large-scale eddies markedly increased as a result of the change of the resolution and coincides very well with the estimates obtained by Starr and White (1954).

The latitude-height distribution of the poleward transport of angular momentum by large-scale eddies in the *N40M* atmosphere is shown in figure 42. In general, this distribution is realistic and reasonable. (For the observed distribution see fig. 6B1 of study S.) There is, however, one curious feature, that is, the equatorward transport of angular momentum by the large-scale eddies in the Tropics. Although such equatorward transport is missing in the annual mean statistics of the angular momentum transport in the actual atmosphere which were obtained by Starr and White (1954), it is evident in the distribution recently obtained by Rasmusson and by Oort (1970). This equatorward transport in the model atmosphere is probably accomplished by tropical disturbances which were discussed in previous sections and in study M2.

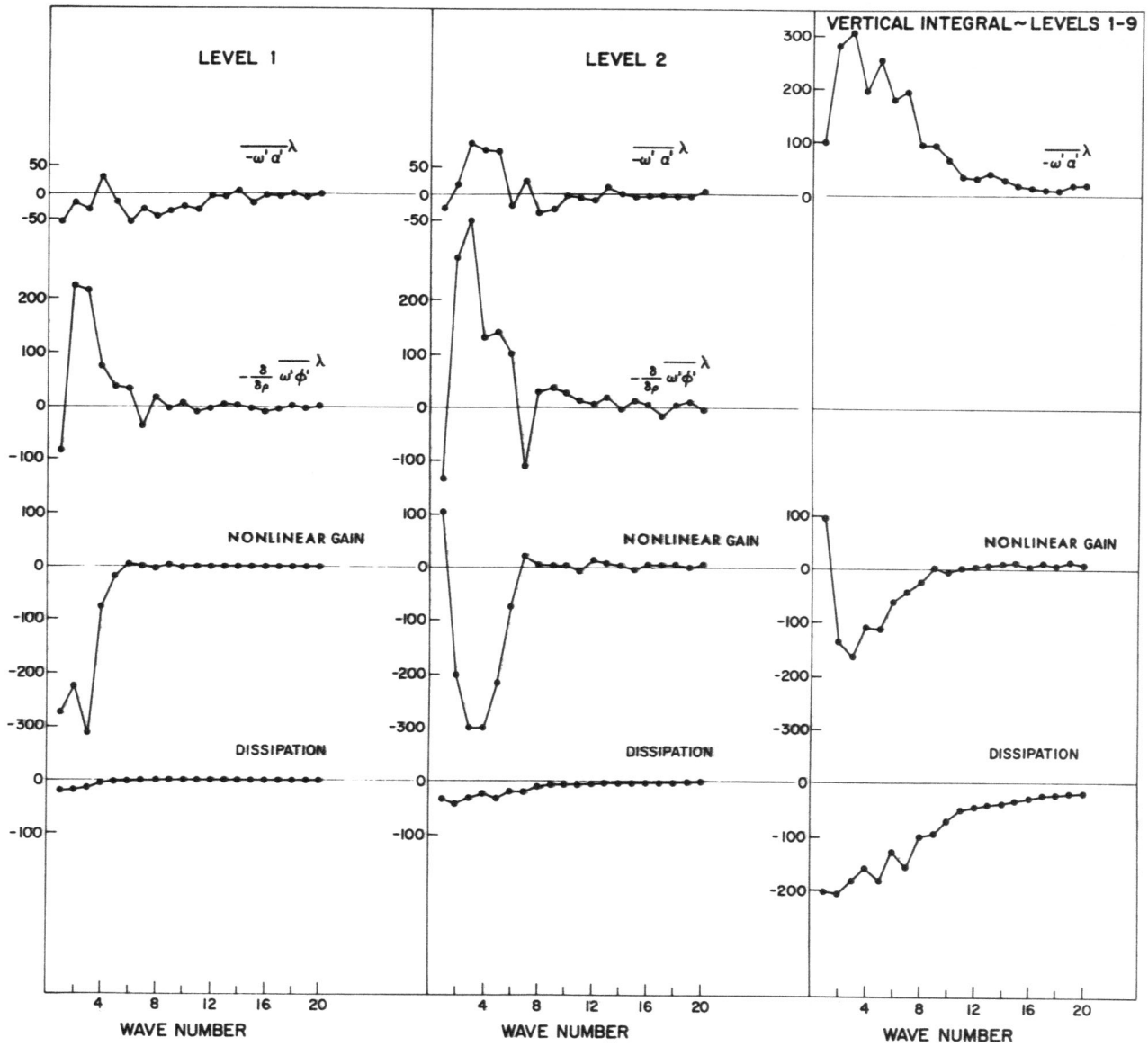

FIGURE 40.—Spectral distributions of the contribution of each term to the rate of change of eddy kinetic energy. Level 1 ($P/P^*=0.009$), level 2 ($P/P^*=0.074$), and the vertical integral of the whole atmosphere. Units, 10^{-3} ergs cm^{-2} mb^{-1} sec^{-1}. Results shown are hemispheric averages.

Budget—The latitudinal distributions of the rates of change of angular momentum in the *N40M* model atmosphere by various factors are shown in figure 43. Poleward of 35° latitude, the contribution of the large-scale eddies and of the surface torque have opposite signs and almost cancel each other. Equatorward of 35° latitude, the meridional circulation plays a significant role and affects the budget of angular momentum together with the large-scale eddies and surface torque.

In order to find out how the distribution of momentum exchange between the earth's surface and the atmosphere is affected by the horizontal resolution of the finite differences, the latitudinal distributions of surface torque in the *N40M* and *N20M* models are compared in figure 44. The corresponding distribution of the *N20D* dry model is also shown. This figure demonstrates that the intensity of momentum exchanges between the earth's surface and the atmosphere is much larger for the *N40M* model than for the *N20M* model at extratropical latitudes. This difference in intensity is consistent with the difference in distributions of zonal mean surface pressure of the two models. As figure 7 indicates, the surface pressure has a much larger latitudinal variation in the *N40M* model than in the *N20M* model. This difference accounts for the difference in the intensity of the surface zonal wind and, accordingly, accounts for the difference in the magnitude of surface torque. As aforementioned, the magnitude of poleward transport of momentum by large-scale eddies

375-632 O - 70 - 4

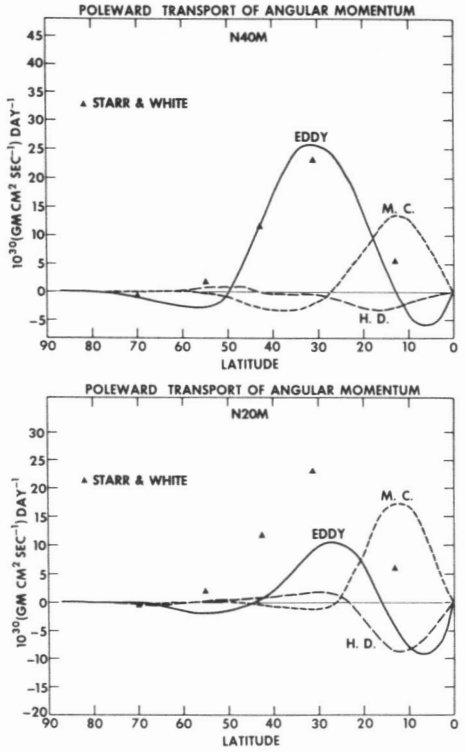

FIGURE 41.—Latitudinal distributions of the poleward transport of angular momentum by large-scale eddies, meridional circulation, and subgrid scale Reynolds stress (H.D.). The rates of the poleward transport of angular atmosphere, estimated by Starr and White (1954), are also plotted.

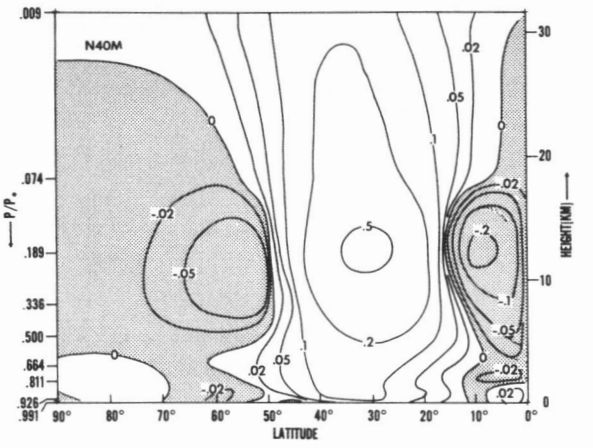

FIGURE 42.—Latitude-height distribution of the poleward transport of angular momentum by large-scale eddies in the *N40M* atmosphere. The region of equatorward transport is shaded. Units, 10^{29} gm cm^2 sec^{-1} day^{-1} mb^{-1}.

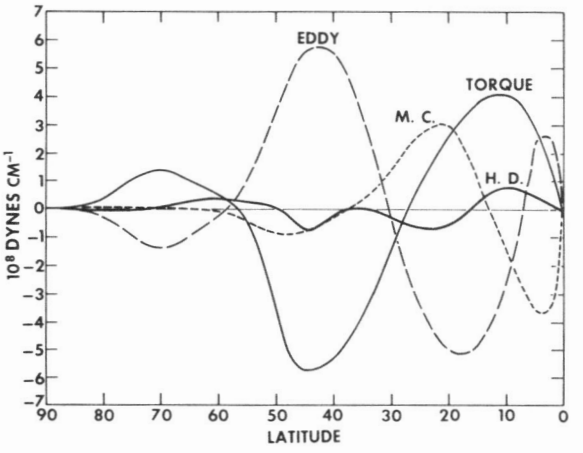

FIGURE 43.—Latitudinal distributions of the rate of change of the angular momentum in the *N40M* atmosphere by meridional circulations, large-scale eddies, subgrid scale horizontal Reynolds stress (H.D.), and surface torque.

increases markedly with increased horizontal resolution. In middle and high latitudes, this increase compensates for the corresponding increase in the magnitude of surface torque mentioned above.

The latitude-height distribution of the rate of change of angular momentum by the meridional circulation, large-scale eddies, and subgrid scale mixing in the *N40M* atmosphere is shown in figure 45. In the boundary layer, the contributions of vertical mixing and meridional circulation almost compensate each other, and the effect of the large-scale eddies is relatively small. In the free atmosphere, large-scale eddies play a major role and have almost the same magnitude but the opposite sign as the meridional circulation. Furthermore, the effects of vertical and horizontal mixing are very small there. A similar feature of the momentum balance was evident in the *N20D* model atmosphere described in study S. Recently, Wiin-Nielsen and Vernekar (1967) investigated the angular momentum balance and found similar characteristics of compensation in the actual atmosphere. Contrasting figure 45 with the upper half of figure 5, which shows the distribution of the zonal mean of the zonal current, we find the following: The momentum transfer by the large-scale eddies contributes toward intensifying the northern half of the tropospheric jet, and the momentum transfer by the meridional circulation helps intensify the southern half of the jet. In the stratosphere, the convergence of angular momentum transport by the large-scale eddies is mainly responsible for the intensification of the jet, while the effect of the meridional circulation weakens the intensity of the jet stream.

B. HEAT

Transport—The latitudinal distributions of the poleward transport of heat by the large-scale eddies and by subgrid scale mixing in the *N40M* and the *N20M* atmospheres are shown in figure 46. Again, the relative magnitude of the transport by the subgrid scale mixing is significantly reduced by the increase of the horizontal resolution, while the heat transport by the large-scale eddies is increased. The percentage increase, however, is not as large as in the case of the angular momentum transport.

In figure 47, the latitude-height distribution of the poleward transport of heat by the large-scale eddies in the *N40M* atmosphere is compared with that in the actual

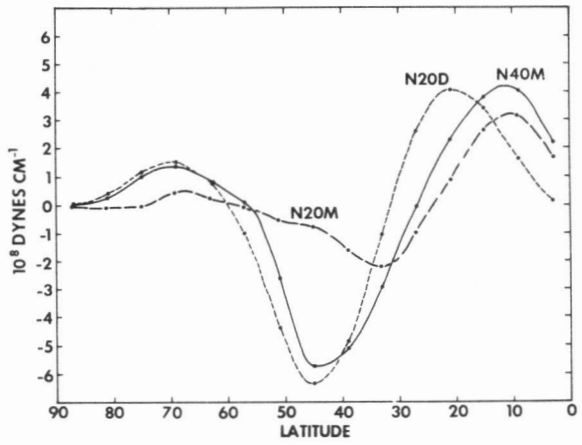

FIGURE 44.—Latitudinal distributions of surface torque for various models.

atmosphere, which was estimated by Starr and White (1954). Although the latitude of maximum poleward transport in the *N40M* model is located to the south of the maximum observed in the atmosphere, there are various features of the model atmosphere distribution that agree with those of the actual atmosphere. For example, the poleward transport in middle latitudes has maxima at two different levels. The primary maximum is located at about the 900-mb level, and a secondary maximum at about the 200-mb level, in agreement with observation. Another interesting feature of the model distribution is the weak equatorward transport of heat in the subtropics. Preliminary analysis of 5 yr of data by Rasmusson and Oort (1970) shows that the actual atmosphere has similar features. A poleward transport of heat, however, appears in the model Tropics.

The latitude-height distribution of the upward transport of heat by the large-scale eddies in the *N40M* atmosphere is shown in figure 48. It has two tropospheric maxima, one in middle latitudes and another in the Tropics. The latitudes of these maxima correspond well with those of the maximum poleward transport of heat which may be identified in the upper part of figure 47. In the subtropics, the vertical transport is very small or even negative. This region of small vertical heat transport corresponds to the region of weak equatorward heat transport by the large-scale eddies mentioned earlier. In the stratosphere of the *N40M* model, downward transport appears, but its magnitude is very small.

Heat balance—The latitudinal distributions of the vertical integral of various heat balance components of the *N40M* atmosphere are shown in figure 49. In the Tropics, the heating by condensation and convection is compensated through the cooling by meridional circulation and radiation. In the subtropics, the heating due to the downward-moving branch of the meridional circulation is counterbalanced mainly by radiative cooling. In middle latitudes, the heat of condensation is mostly compensated by radiative cooling. In high latitudes, the heating resulting from the convergence of the poleward flux of heat by large-scale eddies is compensated mainly by radiative cooling.

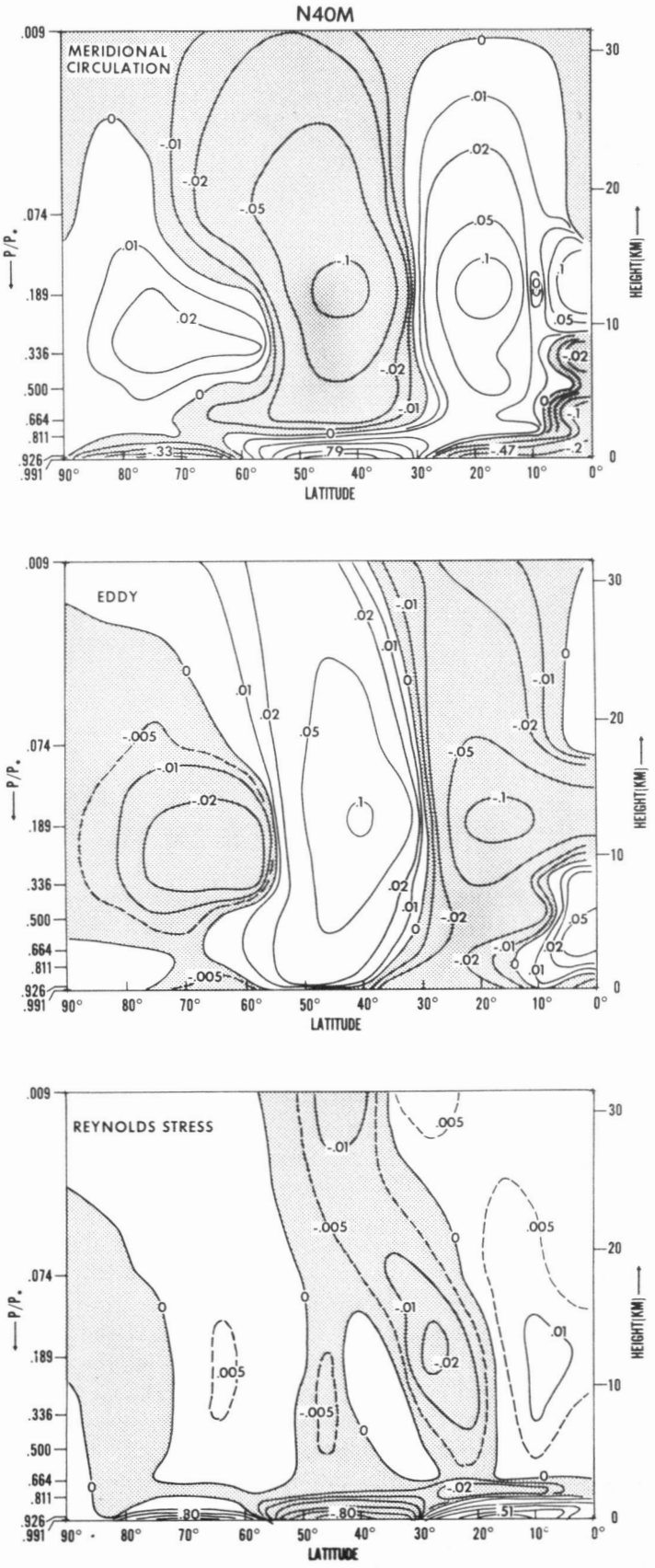

FIGURE 45.—Latitude-height distributions of the rate of change of angular momentum by various components in the *N40M* atmosphere. Units, 10^{12} gm cm^2 sec^{-1} day^{-1} mb^{-1}. Upper third, meridional circulation; middle third, large-scale eddies; lower third, Reynolds stress by vertical and horizontal subgrid scale mixing.

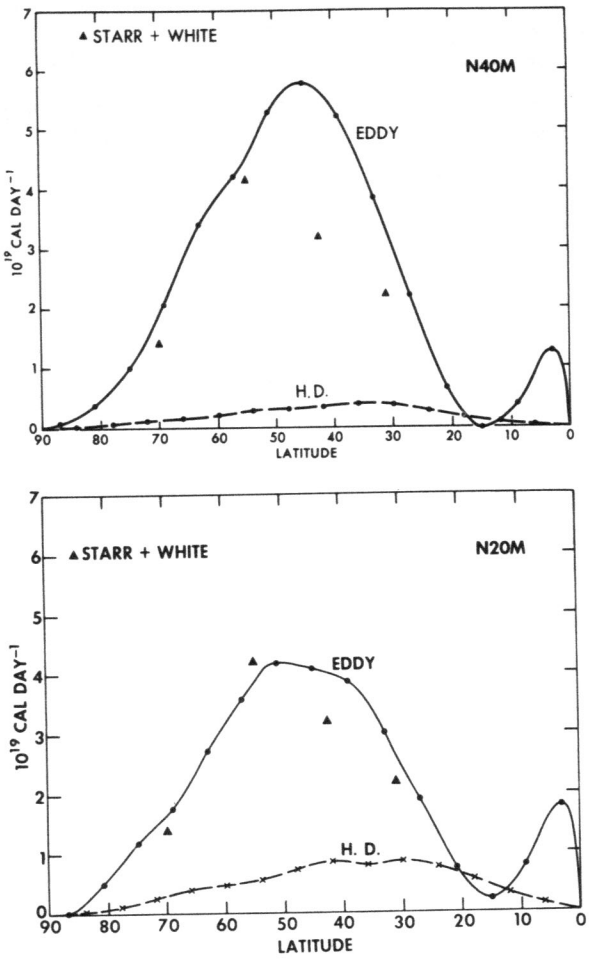

FIGURE 46.—Latitudinal distributions of the poleward transport of sensible heat by the large-scale eddies (Eddy) and by the subgrid scale horizontal mixing (H.D.). Upper half, the *N40M* atmosphere; lower half, the *N20M* atmosphere. The eddy transport values obtained by Starr and White (1954) are also plotted.

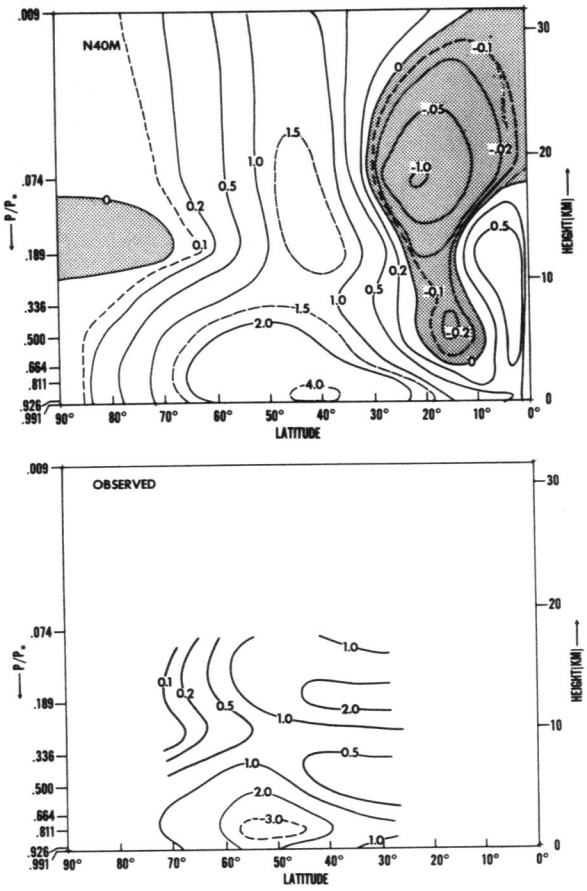

FIGURE 47.—Latitude-height distribution of the poleward transport of heat by the large-scale eddies in units of 10^{17} joules mb^{-1} day^{-1}. Lower half, actual atmosphere (Starr and White 1954); upper half, the *N40M* atmosphere.

The latitude-height distributions of the rate of temperature change due to radiation, condensation and convection, meridional circulation, and large-scale eddies are shown in figure 50. This figure clearly indicates how the heat balance is maintained in the various parts of the atmosphere. For example, the contribution of radiative transfer and condensation is relatively small in the lower stratosphere, while the effect of large-scale eddies has almost the same magnitude but opposite sign as that of the meridional circulation. As previously discussed, the stratospheric flow field is not driven by the meridional heating contrast but by the energy flow from the troposphere. This is why a significant level of eddy kinetic energy is maintained there, despite the weak heating contrast. The relationships between the thermal structure of the stratosphere and the various thermodynamical factors were discussed extensively by Manabe and Hunt (1968) and will not be repeated here.

In the troposphere of the *N40M* model, the rate of temperature change due to condensation and convection has a distinct double maximum, one in the Tropics and another in middle latitudes. The former is caused by the tropical rain belt, and the latter is maintained by the middle-latitude rain belt. As one would expect, the heating due to moist convection and condensation penetrates much higher in the Tropics than in middle latitudes.

The mass integrals of various heat balance components have been embodied into box diagrams for both the *N40M* and the *N20M* atmospheres. These are shown in figure 51. We see that the heat balance of the hemisphere as a whole depends slightly upon the resolution of the horizontal finite differences. However, the rate of heat released by condensation is larger in the *N40M* atmosphere than in the *N20M* atmosphere.

C. WATER

Transport—The latitudinal distribution of the poleward transport of moisture by the meridional circulation, large-scale eddies, and by subgrid scale mixing in both the *N40M* and the *N20M* atmosphere are compared in figure 52. The poleward transport of moisture by large-scale eddies is affected slightly by the change of horizontal resolution, although in middle latitudes the eddy transport is slightly

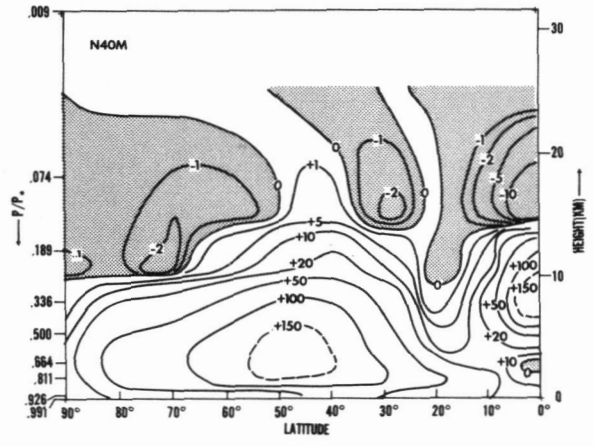

FIGURE 48.—Latitude-height distribution of upward transport of heat by large-scale eddies in the *N40M* atmosphere. Units, joules cm^{-2} day^{-1}.

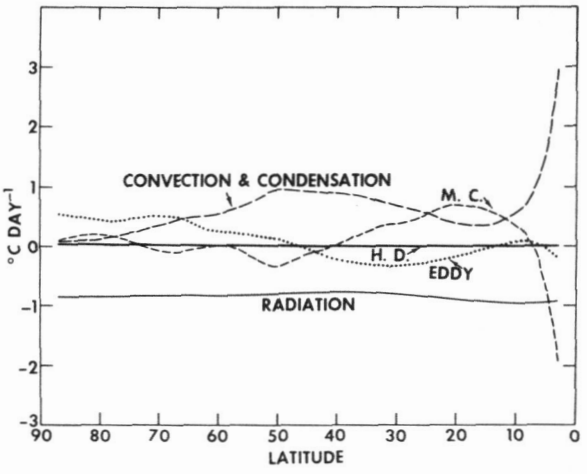

FIGURE 49.—Latitudinal distributions of the vertical mean temperature changes, which are due to radiation, heat of condensation and convection, meridional circulation, large-scale eddies, and subgrid scale diffusion (H.D.) in the *N40M* atmosphere.

larger in the *N40M* than in the *N20M* atmosphere. It is rather interesting that the degree of the dependence upon the horizontal resolution is not the same for momentum, heat, or moisture transport by the large-scale eddies. The moisture transport is least affected.

The poleward transport of moisture by the indirect meridional circulation cell in middle latitudes increases significantly as a result of the intensification of this cell caused by the change of resolution; whereas, the equatorward transport by the tropical Hadley cell is affected only slightly. The poleward transport of moisture by the subgrid scale mixing decreases significantly as a result of the change of the horizontal resolution, as was also the case with heat and momentum.

The latitude-height distributions of the poleward transports of moisture by the large-scale eddies and by the meridional circulation are shown in figure 53. It is interesting that the direction of the eddy transport of moisture in the model stratosphere is opposite in the model troposphere. In the stratosphere, moisture is transported equatorward. The moisture balance of the stratosphere has already been discussed in the study M. Refer to study M for further details of water balance in the model stratosphere.

Budget—The latitudinal distributions of precipitation and evaporation of the *N40M* and the *N20M* atmospheres are shown in figure 54. This figure shows that the difference between these distributions in the two models is rather small. Therefore, we shall describe the water balance of the *N40M* model only. The latitudinal distributions of various water balance components are shown in figure 55. In the Tropics, the moisture supplied by the meridional circulation and by evaporation is consumed by the precipitation of the tropical rain belt. In the subtropics, the moisture gained by evaporation is removed mainly by meridional circulation. In middle latitudes, moisture supplied by evaporation and large-scale eddies is precipitated in the middle-latitude rain belt. In high latitudes, the influx of moisture by the large-scale eddies is counterbalanced by precipitation.

Finally, the hemispheric water balance of both models is tabulated in figure 56. Again, this table indicates that the intensity of the hydrologic cycle in the *N40M* model is slightly greater than in the *N20M* model. In general, the magnitude of vertical motion is larger in the *N40M* than in the *N20M* atmosphere. The difference in the intensity of vertical mixing of moisture by large-scale eddies may be responsible for the difference in the intensity of the hydrologic cycle mentioned above.

D. EDDY TRANSPORT IN DRY MODELS AND MOIST MODELS

In the preceding subsections, we have compared the distributions of the poleward transport of angular momentum, heat, and moisture by large-scale eddies in the *N40M* atmosphere with those in the *N20M* atmosphere. In this subsection we shall compare some of these distributions with those in the dry model (*N20D* and *N40D*) atmospheres, because dry models are widely used for various purposes. Figure 57 shows the latitudinal distributions of the poleward transport of angular momentum by large-scale eddies in the four different model atmospheres. This figure demonstrates that the magnitude of the poleward transport of angular momentum is influenced very markedly by the incorporation of the hydrologic cycle as well as by the change in the horizontal resolution. The magnitude of the poleward eddy transport of angular momentum in the *N20D* model atmosphere happens to be very realistic because the poor horizontal resolution compensates for the absence of the hydrologic cycle. Accordingly, further improvement of the horizontal resolution results in a very large and highly unrealistic magnitude of transport in the *N40D* atmosphere. In short, we obtained superficially realistic results from

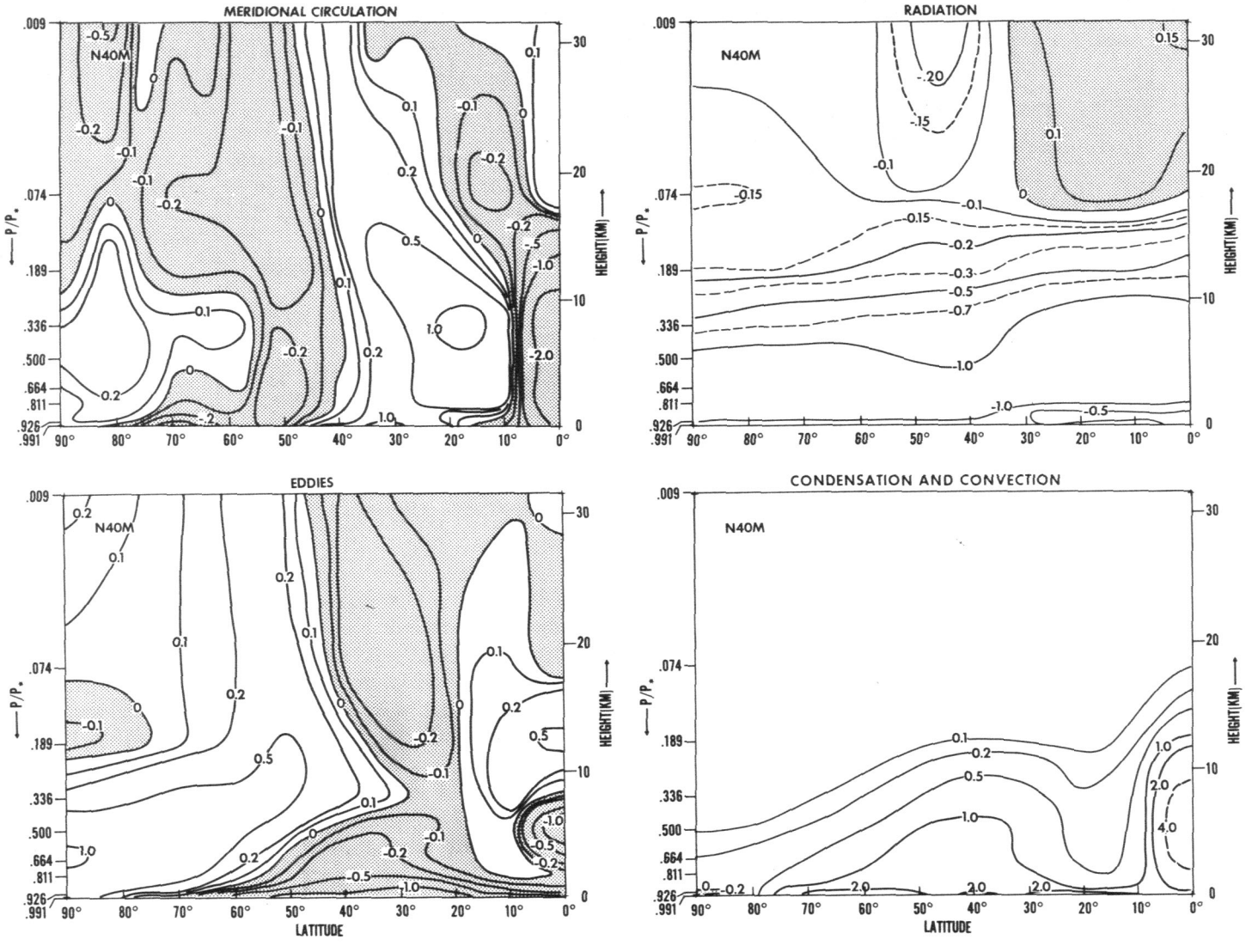

FIGURE 50.—Latitude-height distributions of the rates of temperature change which are due to various components of the heat balance (°C day^{-1}) in the *N40M* atmosphere.

an unrealistic model. Under these circumstances, it is highly desirable to perform integrations with still higher resolutions (say *N80M*) to make sure that the *N40M* results are asymptotically stable.

The latitudinal distributions of the poleward transport of heat by large-scale eddies in the various model atmospheres are also shown in figure 58. Note that the incorporation of the hydrologic cycle significantly affects the magnitude of the poleward transport of heat. The poleward transport of latent energy contributes to a reduction in the meridional temperature gradient in the moist atmospheres compared with dry models and, accordingly, the rate of poleward eddy transport of sensible heat is reduced. It is noteworthy, however, that the doubling of the resolution from *N20* to *N40* has as much effect upon the poleward transport of heat as the moist process does.

8. BUDGET OF ENERGY

It is known that the zonal kinetic energy in the atmosphere is maintained against dissipation mainly by the nonlinear barotropic transfer of energy from the large-scale quasi-two-dimensional eddies to the zonal current (Starr 1953). Such a transfer of energy is evident in the energy diagram for the actual atmosphere, which has been compiled by Oort (1964*b*) and shown in figure 60. The corresponding energy diagram for the *N20M* atmosphere (fig. 59) shows that the flow of kinetic energy is in the opposite direction, that is, the zonal kinetic energy is transferred into eddy kinetic energy. The zonal kinetic energy is maintained against dissipation by the conversion of the zonal potential energy into zonal kinetic energy. As discussed in section 6, this unrealistic feature of the energy transfer is attributed mainly to the excessive subgrid scale dissipation operating in this coarse resolution moist model.

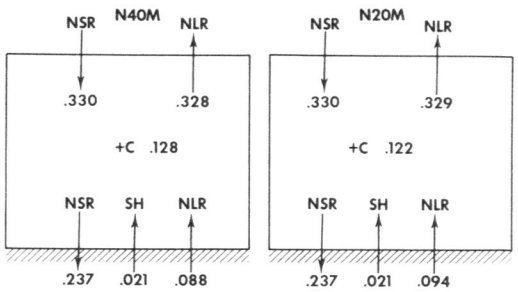

FIGURE 51.—Box diagrams of heat balance of the *N40M* and the *N20M* atmosphere. The lower and upper boundaries of the boxes indicate the earth's surface and the top of the atmosphere, respectively; NSR, net solar radiation; NLR, net long wave radiation; SH, sensible heat flux from the earth's surface; C, heat of condensation. Units, ly min^{-1}.

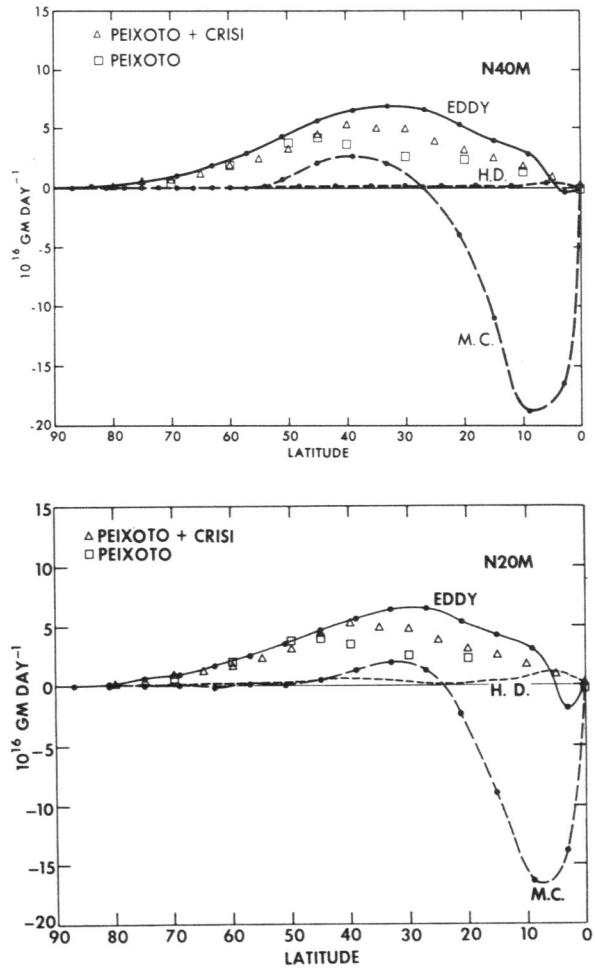

FIGURE 52.—Latitudinal distributions of the poleward transport of moisture by meridional circulation, large-scale eddies, and subgrid scale diffusion (H.D.). The estimates of the annual mean poleward transport in the actual atmosphere obtained by Peixoto (1958) and Peixoto and Crisi (1965) are also plotted. Upper half, *N40M* atmosphere; lower half, *N20M* atmosphere.

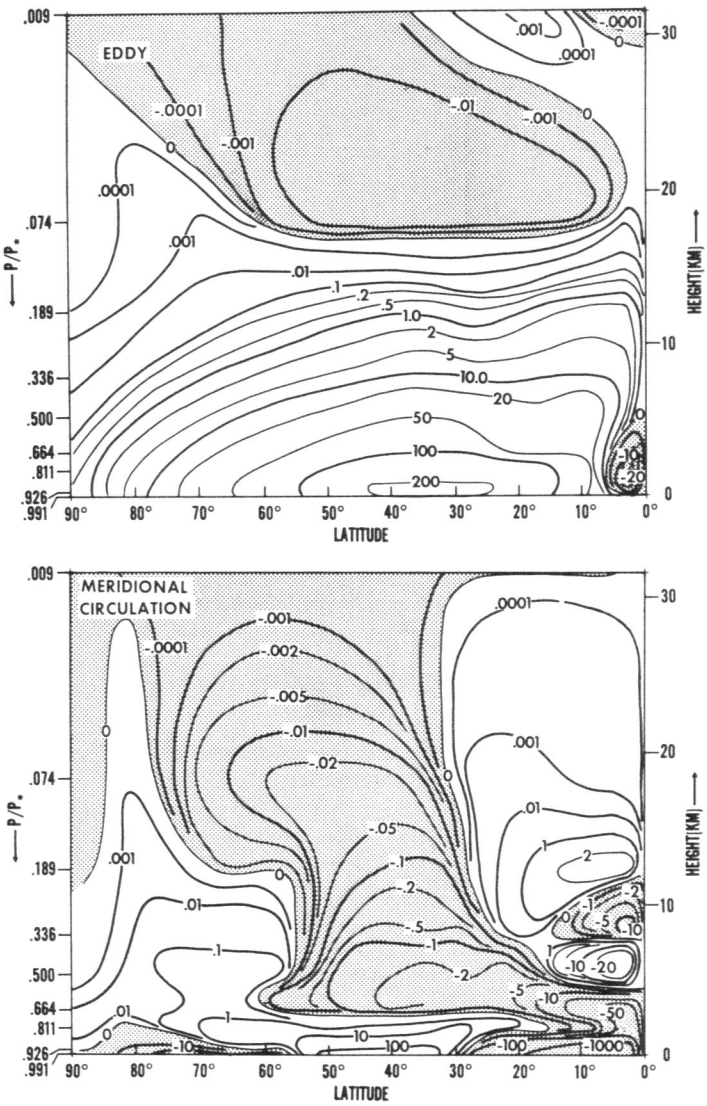

FIGURE 53.—Latitude-height distribution of the poleward transport of water vapor in the *N40M* atmosphere. Upper half, transport by large-scale eddies; lower half, transport by meridional circulation. Units, 10^{12} gm mb^{-1} day^{-1}.

In the *N40M* atmosphere, where the effect of the horizontal subgrid scale mixing is less dominating and where the barotropic net energy exchange is of significant magnitude, energy is transferred from eddy to zonal kinetic energy and contributes to the maintenance of zonal kinetic energy in agreement with the behavior of the actual atmosphere. This is one of the most fundamental improvements resulting from the increased horizontal resolution.

One of the interesting features of the energy balance of the moist model atmosphere is the conversion from zonal potential to zonal kinetic energy. Although the zonal conversion in the *N40M* atmosphere is smaller than that of the *N20M* model, there is no doubt that it has a positive value with significant magnitude. In the dry model atmospheres (Phillips 1956, Smagorinsky 1963, *N20D* and *N40D* atmospheres), energy is transferred from zonal kinetic energy to zonal available potential energy. This negative conversion is particularly large in the *N40D*

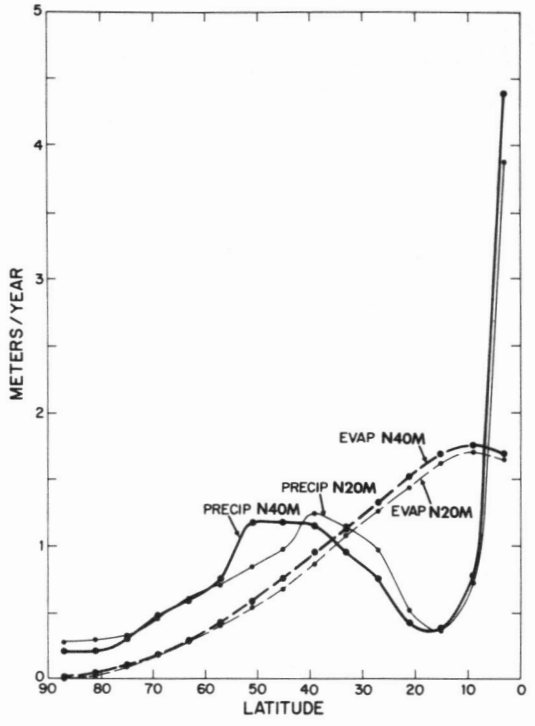

FIGURE 54.—Latitudinal distributions of the rates of precipitation and evaporation.

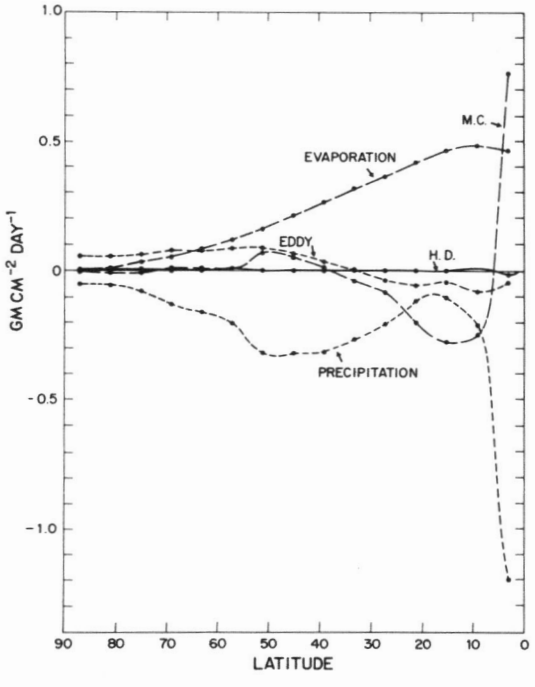

FIGURE 55.—Latitudinal distributions of the various water balance components of the *N40M* atmosphere, that is, condensation, evaporation, meridional circulation, large-scale eddies, and subgrid scale horizontal mixing (H.D.).

atmosphere. As it is evident in table 3, which shows the intensity of meridional circulations in both the dry and the moist models, the condensation process helps to intensify the direct tropical cell and weaken the indirect Ferrel cell in middle latitudes. As pointed out in study M, the heat of condensation released in the upward branch of

	PRECIPITATION	EVAPORATION
N40M	.3109	.3073
N20M	.2980	.2925

FIGURE 56.—Table of hemispheric water balance at the earth's surface. Units, cm day^{-1}.

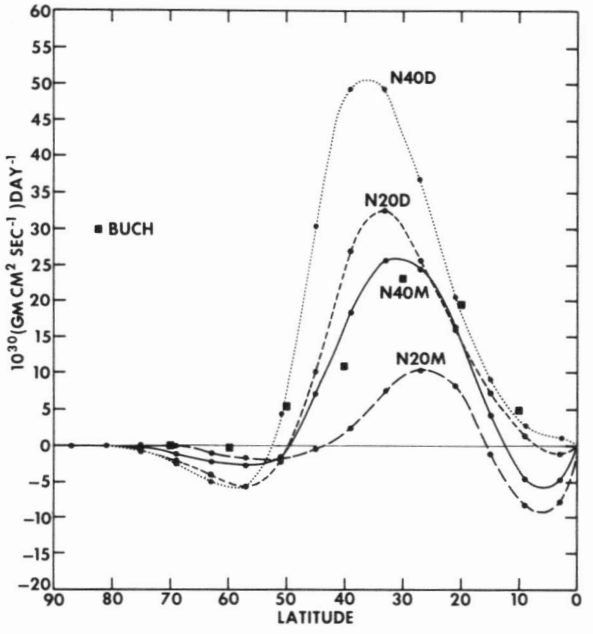

FIGULE 57.—Latitudinal distributions of poleward transport of angular momentum by the large-scale eddies in various models. The rates of transport in the actual atmosphere, which were obtained by Buch (1954), are also plotted.

the Hadley cell is expected to increase the intensity of the cell. Also, the poleward transport of latent energy acts to reduce the meridional temperature gradient and, accordingly, the degree of baroclinic instability which drives the indirect Ferrel cell. Both of these changes caused by moist processes help to increase the release of zonal available potential energy into zonal kinetic energy and prevent the zonal conversion in the moist atmospheres from becoming negative.

It is very difficult to estimate the value of the zonal conversion in the actual atmosphere because the wind components involved in the meridional circulation are very small. According to the energy diagram, compiled by Oort (1964*b*) and shown in figure 60, this conversion has a small positive value, although the accuracy of his estimate of this determination is so unreliable that small negative values are within the limits of the probable dispersion in the estimate. As described previously, the zonal conversion of potential energy in the *N40M* atmosphere has a positive value of significant magnitude and contributes to the maintenance of zonal kinetic energy. Although it is not certain whether the positive conversion of such magnitude takes place in the actual atmosphere, it is

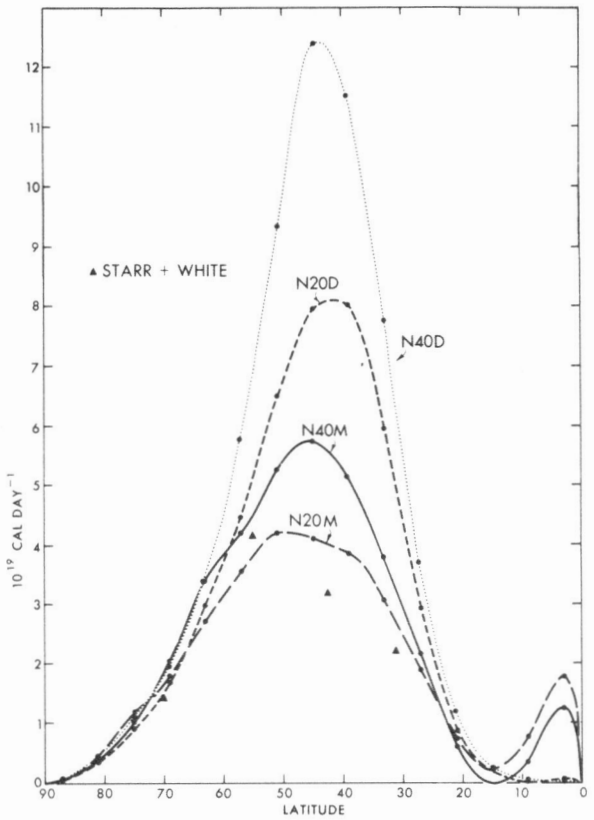

FIGURE 58.—Latitudinal distributions of poleward transport of sensible heat by the large-scale eddies in various models. The rates of transport in the actual atmosphere, which were obtained by Starr and White (1954), are also plotted as solid triangles.

highly unlikely that the zonal conversion in the actual atmosphere has such a large negative value as does the *N40D* atmosphere because of condensation. In view of the significant difference between the magnitudes of the zonal conversion in the *N40M* and the *N20M* atmosphere and in view of the highly idealized nature of the lower boundary conditions chosen for the present model, it is desirable to reevaluate this term after further improvement of the model.

Another notable feature of the energy diagram of the moist model is the large generation of the eddy available potential energy due to condensation and convection. In the moist model atmospheres, the eddy available potential energy is maintained despite its large conversion into eddy kinetic energy by the following processes:

1) The transfer of the zonal available potential energy into the eddy available potential energy.

2) Generation of the eddy available potential energy by heat of condensation and convection.

Comparing the energy diagram of the dry *N40D* model with the energy diagram of the moist *N40M* model, we find that the conversion of zonal to eddy available potential energy in the *N40D* atmosphere is larger than in *N40M* and *N20M*, compensating for the lack of eddy generation by the heat of condensation and convection.

Figure 61 shows the latitude-height distribution of the rate of generation of available potential energy by the heat of condensation and convection in the *N40M* atmosphere. According to this figure, there are two regions of large generation, one in middle latitudes and another in the Tropics. Figure 62 is a schematic illustrating a typical developing cyclone in middle latitudes. In such a cyclone, a thermal trough is located to the west of a pressure trough. Since condensation usually takes place eastward of the trough, a positive correlation exists between the heat of condensation and temperature. Accordingly, the heat of condensation generates eddy available potential energy in middle latitudes. The mechanism for generating eddy available potential energy in the model Tropics is somewhat different in middle latitudes and is extensively discussed in study M2. In the model Tropics, the eddy available potential energy is generated by the heat of condensation, which is released in tropical cyclones with warm cores in the upper troposphere. According to our crude estimate, the generation in the middle latitudes accounts for two-thirds of the total eddy generation and the generation in the Tropics covers the remainder. It is probable that the eddy generation due to condensation has a significant magnitude in the actual atmosphere, although the energy diagram of Oort suggests otherwise.

Finally, the energy budget of the stratosphere of the *N40M* astmosphere is shown in figure 63. The major source of eddy kinetic energy in the stratosphere comes from the troposphere through the pressure interactions ($\overline{-\omega'\phi'}^{\lambda}$). The major sink of eddy kinetic energy is the transfer to zonal kinetic energy which in turn is converted into zonal potential energy. The zonal potential energy is destroyed by radiative damping (Q_R) or transferred into eddy potential energy. Qualitatively, similar features were found for the dry general circulation model discussed in study S. In summary, the major source of energy in the stratosphere is the troposphere rather than an in situ conversion of potential energy, and the major consumption of energy is accomplished by the radiative damping of the zonal available potential energy as well as by the dissipation of kinetic energy. There is one significant difference between the energy budget of the *N40M* stratosphere and the energy budget of the actual stratosphere which was determined by Oort (1964*a*). In the model atmosphere, energy is transferred from zonal to eddy available potential energy, whereas the reverse is true in the actual atmosphere. This discrepancy is related to insufficient poleward heat transport by large-scale eddies and, accordingly, to the insufficient increase of temperature with increasing latitude in the lower stratosphere. Recently, Manabe and Hunt (1968) performed an integration with a dry general circulation model with a high vertical resolution and successfully obtained a sufficient latitudinal increase of temperature. In their model atmosphere, a countergradient poleward flux of heat by the large-scale eddies predominates, and energy transfer of significant magnitude from eddy to zonal available potential energy is maintained in agreement with observation. Therefore, an increase of vertical resolution seems to be necessary for a satisfactory simulation of the energetics of the stratosphere.

375-633 O - 70 - 5

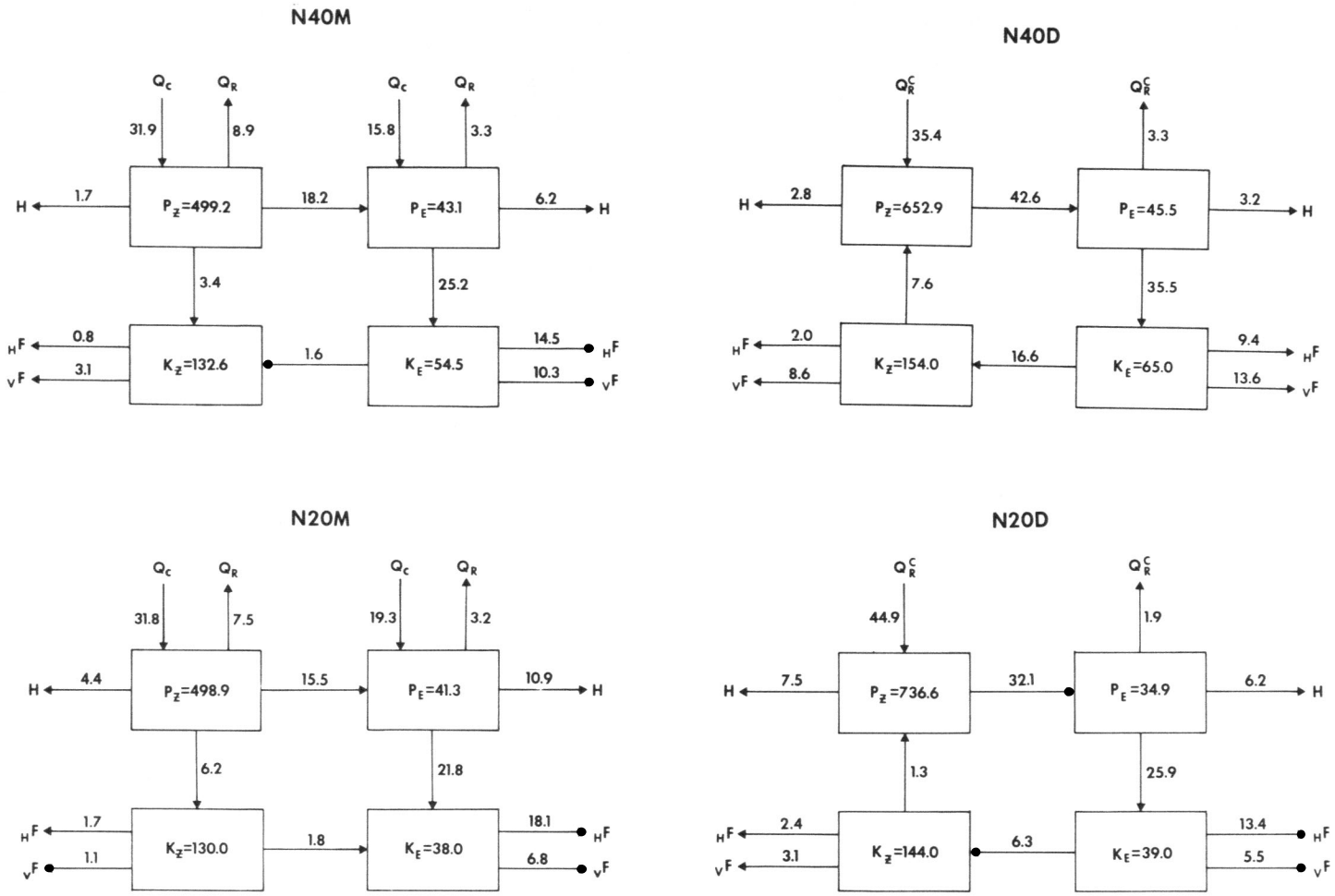

FIGURE 59.—Box diagrams of energetics of the various model atmospheres. Q_C, generation of available potential energy by condensation and convection (here, convection includes the sensible heat flux from the earth's surface); Q_R, generation of available potential energy by radiation; Q_R^C, sum of Q_R and Q_C; H, destruction of available potential energy by the horizontal subgrid scale mixing; $_HF$, destruction of kinetic energy by the horizontal, subgrid scale mixing; $_VF$, destruction of kinetic energy by the vertical subgrid scale mixing. Units of exchange, 10^{-3} joules cm^{-2} mb^{-1} day^{-1}; units of energy (in boxes), joules cm^{-2}. See study S for the mathematical expression of the transfer term.

9. SUMMARY AND CONCLUSIONS

The decrease of the horizontal grid size from 500 to 250 km increases the accuracy of the dynamical computation. For example, in the low resolution *N20M* model, the fronts are not very sharp and the bands of frontal rain are wide and diffuse. On the other hand, the surface fronts in the high resolution *N40M* model have highly realistic structures. They are characterized by dense concentrations of isotherms, narrow bands of frontal rain, and associated cyclone families. Further reduction in the horizontal grid size seems to be desirable in order to resolve sufficiently the structure of cyclone families.

The comparison between the atmospheres with and without the effects of the selective heating of condensation indicates that the moist processes are responsible for sharpening the fronts and reducing the scale of cyclones in the lower troposphere. In the dry model atmosphere, the characteristic scale of the cyclones near the earth's surface is comparable with that at the 500-mb level; whereas in the moist model atmosphere, the scale of low-level cyclones is significantly smaller than that of the disturbances in the upper troposphere.

According to an harmonic analysis, the dissipation of eddy kinetic energy by horizontal subgrid scale viscosity prevails not only at the grid scale but also at larger scales. Since the scale at which the horizontal dissipation is most effective decreases with decreasing grid size, the eddy kinetic energy of the large-scale disturbances is dissipated more effectively in the low resolution *N20M* atmosphere than in the high resolution *N40M* atmosphere. In the *N20M* atmosphere, the total dissipation, which is the sum of the horizontal and the vertical dissipation, is almost equal to the rate of conversion from potential to kinetic energy at each wave number. Accordingly, there is

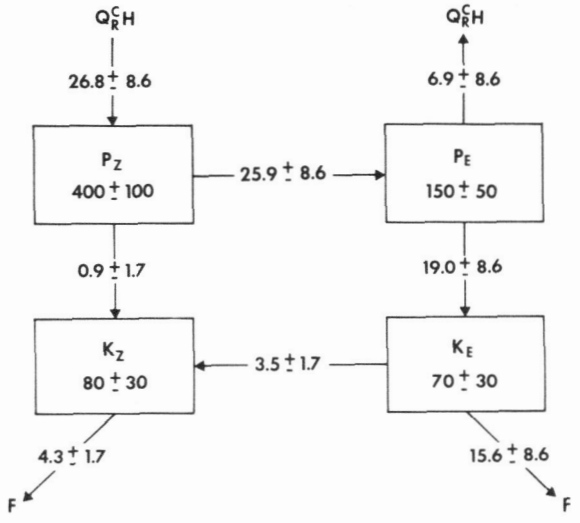

FIGURE 60.—Box diagram of energetics of the actual atmosphere compiled by Oort (1964*b*). $Q_R^C H$, sum of Q_R, Q_C, and H; for a further explanation, see figure 59.

TABLE 3.—*Intensity of meridional circulations (units, 10^{12} gm sec^{-1})*

	Model			
	N40M	*N20M*	*N40D*	*N20D*
Hadley cell, Tropics	153	125	77	67
Ferrell cell, midlatitudes	36	22	71	42
Polar cell	5	2	8	6

little net transfer of energy between eddies of different scales. In the *N40M* atmosphere, the rate of total conversion is somewhat greater than the dissipation rate at medium wave numbers. The excess energy converted at medium wave numbers is for the most part transferred barotropically to very long waves and to the zonal current. This comparison between the energetics of the two model atmospheres indicates that the horizontal viscosity tends to dissipate the kinetic energy of large-scale eddies which should otherwise be transferred to eddies with lower wave numbers through the barotropic process. Furthermore, it should be noted that the rate of conversion of potential energy at lower wave numbers is much larger in the *N40M* atmosphere than in the *N20M* atmosphere which probably results from the difference in the character of the horizontal dissipation mentioned above. Owing to the differences in the spectral distributions of dissipation, conversion, and barotropic energy exchange, the kinetic energy is larger and more realistic in the *N40M* atmosphere than in the *N20M* atmosphere at low as well as high wave numbers.

Since the scales of horizontal dissipation overlap with those of conversion from potential to kinetic energy as indicated above, the horizontal nonlinear viscosity is not operating in the inertial subrange for which it was designed. Furthermore, the typical inertial subrange of

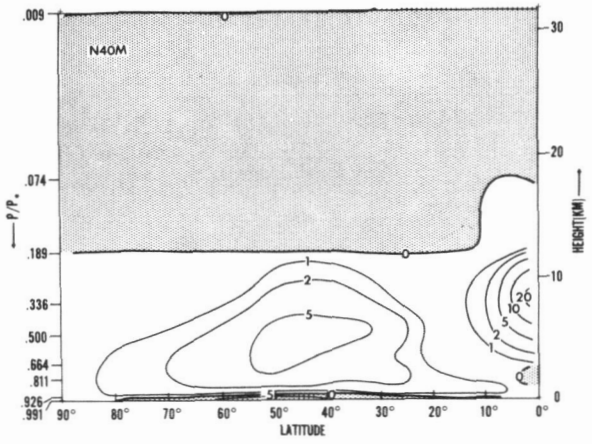

FIGURE 61.—Latitude-height distribution of the rate of generation of available potential energy by condensation and convection in the *N40M* atmosphere. Units, ergs cm^{-2} sec^{-1} mb^{-1}.

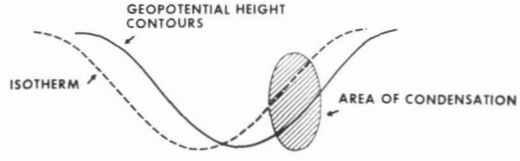

FIGURE 62.—Schematic illustrating a typical developing cyclone in middle latitudes.

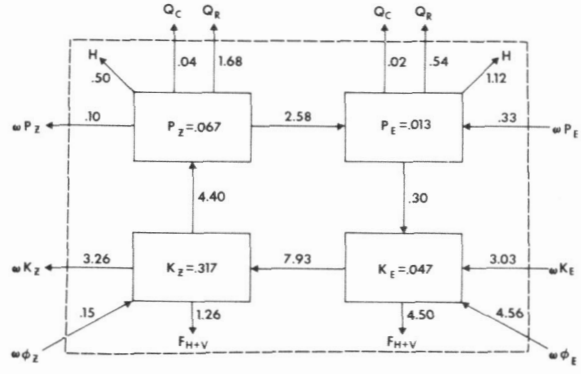

FIGURE 63.—Box diagram illustrating the energetics of the stratosphere of the *N40M* model. Units of energy (in boxes), joules cm^{-2} mb^{-1} (see fig. 59 for details).

three-dimensional eddies should not be realized at grid scale in any event because the horizontal mesh interval is much larger than the equivalent depth of the atmosphere. Recently, Leith (1969) proposed a formulation of a horizontal eddy viscosity based upon the dimensional analysis of two-dimensional turbulence. Since his version of nonlinear viscosity is more scale-selective than the one adopted for this study, the choice of his formulation should decrease the dissipation of synoptic scale eddies. Whichever formulation we may use, it seems to be highly desirable to increase the resolution of horizontal finite differencing further. Such an increase not only improves

the accuracy of the horizontal finite differencing but also separates the scale of subgrid scale dissipation from the scales of baroclinic instability.

Another alternative is to represent the equation of motion by spherical harmonics as Platzman (1960) proposed and systematically truncate the higher wave number components, thereby avoiding the explicit use of horizontal viscosity. One can show that such systematic truncation of the series does not deplete kinetic energy from the system. According to Kraichnan (1967), a two-dimensional cascade of energy at wave numbers higher than those of the energy source does not exist when the energy spectrum has attained the equilibrium distribution. It was shown that such a cascade is very small in the *N40M* atmosphere. Therefore, the use of orthogonal functions may be one of the attractive ways to avoid this difficulty.

A major emphasis of this study was a detailed analysis of the various components of energy transfer in the moist model atmospheres. In the *N20M* model, the decascade of eddy to zonal kinetic energy is missing because of the domination of the horizontal eddy viscosity. On the other hand, in the *N40M* model energy is transferred from the eddy to the zonal kinetic energy in agreement with the actual atmosphere. It is noteworthy that the energy conversion from zonal available potential energy also plays a significant role in maintaining the zonal kinetic energy of the moist model atmosphere.[3] In the dry model atmospheres, the zonal conversion is negative and depletes the zonal kinetic energy. The difference between the dry and the moist models is due to the difference in the intensity of the Hadley cell in the Tropics and the Ferrel cell in middle latitudes.

Another interesting outcome of the energy analysis of the moist model atmosphere is the large generation of the eddy available potential energy by the heat of condensation. In the dry model atmospheres, the eddy available potential energy is produced solely by the transfer of energy from the zonal available potential energy. On the other hand, in the moist model atmosphere the eddy generation by the heat of condensation has a magnitude comparable with the supply of energy from the zonal available potential energy.

A detailed analysis of the energetics of the *N40M* atmosphere in wave number space reveals essential differences between the energy budgets of various parts of the atmosphere. In the model troposphere, eddy kinetic energy is produced by the conversion of eddy potential energy in the range of wave numbers 2 to 8. Some of the energy thus produced is dissipated, but most of the remainder is transferred to zonal kinetic energy. In the stratosphere, where very long waves predominate, eddy kinetic energy is generated in the 2 to 3 wave number range, mainly as a result of the pressure interaction with the underlying troposphere. Some of the eddy kinetic energy is then transferred to the zonal kinetic energy by means of a barotropic nonlinear decascade. It is very interesting that the magnitude of the transfer toward higher wave numbers is extremely small as compared with the magnitude of the transfer toward low wave numbers.

In the Tropics, the eddy kinetic energy is produced mainly by the release of eddy available potential energy generated by the heat of condensation. Although the rate of conversion is a maximum at very low wave numbers, the conversion spectrum extends to very large wave numbers.

In conclusion, the dynamical structure of the moist model atmosphere becomes highly realistic as a result of the reduction of the grid size, which in midlatitudes is approximately from 500 to 250 km, although further increase of the resolution of horizontal finite differences seems to be desirable.

APPENDIX I—SCHEME OF NUMERICAL TIME INTEGRATION

The time step for integration of the *N40M* model was 5 min, half that used in the *N20M* and *N20D* models. In order to prevent the growth of the computational mode, the wind, temperature, humidity and pressure fields at three consecutive time steps were averaged by the weights 0.25, 0.5, and 0.25 every 53 time steps. After such a smoothing time step, one noncentral time extrapolation was performed before the normal "leapfrog" time integration was resumed.

In spite of this periodic time smoothing, the *N40M* model developed high-frequency external gravity waves in the Tropics which were not present in the low resolution model experiments. Apparently, the irregular boundary at the Equator excited these surface-pressure disturbances because they appeared first as meridional bands radiating poleward from the roughest sections of the boundary. The reason why these occur only at high resolution has never been determined.

The most effective technique for suppressing these gravity waves was to use the so-called Euler backward time-differencing method (see, for example, Matsuno 1966) periodically in place of the normal leapfrog procedure until these unwanted disturbances were reduced to insignificant amplitude. This method consists of a two-pass procedure in which tentative next-time step values of the predictands are obtained from which definitive rates of change are derived for computing the final values by noncentral time extrapolations. Let V represent a typical predictand, then

$$V^* = V^\tau + \Delta t \cdot \left(\frac{\partial V}{\partial t}\right)^\tau \text{ (first pass)}$$

and

$$V^{\tau+1} = V^\tau + \Delta t \cdot \left(\frac{\partial V}{\partial t}\right)^* \text{ (second pass),}$$

where the superscripts denote the time level, τ is the time

[3] Since the free-slip equatorial wall could affect the intensity of the Hadley cell, it is desirable to reevaluate this conclusion by use of a model without such a wall.

step number, the asterisk indicates the tentative estimate of the predictand, and Δt is the length of the time step.

During the time integration of the high resolution models, this Euler backward procedure was carried out every 1,008 time steps for a series of 143 consecutive time steps. Furthermore, during the application of this method, the time step was reduced from 5 min to 135 sec because this Δt was found by trial and error to be the longest time step that was effective in smoothing out the gravity waves, which in the *N40M* model had a mean period of about 15 min. While this method was being used, forecast time thus advanced at less than one-quarter of the normal speed.

APPENDIX II—BRIEF DESCRIPTION OF THE DRY GENERAL CIRCULATION MODEL

In view of the frequent reference to the dry model in the manuscript, a brief description of the dry model is appropriate. The basic difference between the dry and moist model is that the former does not contain moisture processes, that is, transport of moisture, condensation and evaporation, whereas the latter model does. For example, the effects of selective heating by the condensation process and the poleward transport of latent energy are absent in the dry model but are present in the moist model.

The effect of the moist convection, however, is incorporated into the dry model in a very crude manner in order to prevent the lapse rate from becoming too unrealistic. It consists of adjusting the lapse rate to the moist adiabatic value wherever the lapse rate exceeds this critical value. For further details of the structure of the dry model, see study S.

The initial conditions for the numerical time integration of the *N40D* model is the state of the moist atmosphere at the 200th (moist) model day. The period of integration is 70 model days. The last 30 days of this integration period is chosen for the analysis. Various quantities of the *N40D* model shown in this study represented the average value for this 30-day period unless we specified otherwise.

The latitude-height distributions of the zonal mean of zonal wind and eddy kinetic energy are shown in the upper and lower parts of figure 64. According to this figure, the intensity of the zonal current in the *N40D* model is unrealistically strong. The eddy kinetic energy of this model is much larger than that of the *N40M* model. This result partially explains why the eddy transports of the various quantities in the *N40D* atmosphere are very large. (See study S for the description of the *N20D* atmosphere.)

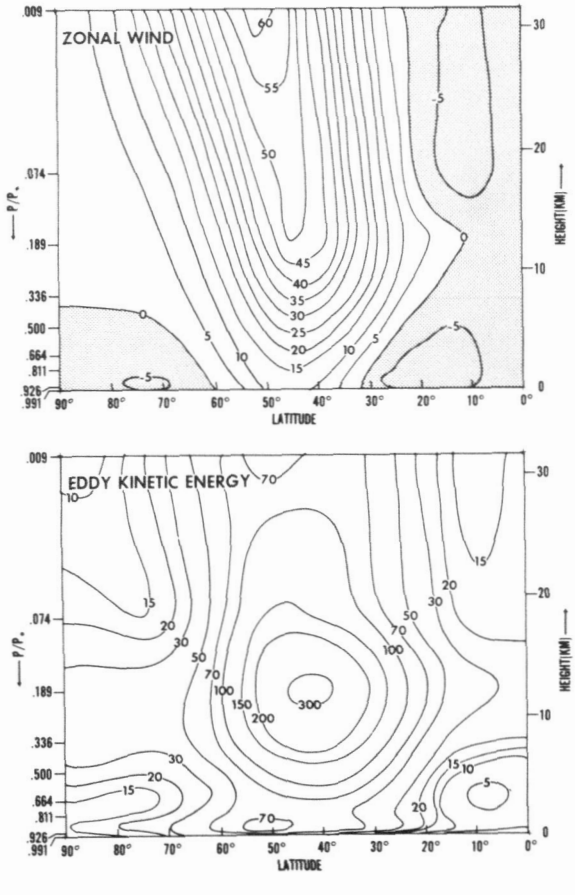

FIGURE 64.—Upper half, latitude-height distribution of the zonal mean of zonal wind in the *N40D* atmosphere (units, m sec^{-1}); lower half, latitude-height distribution of eddy kinetic energy in the *N40D* atmosphere (units, 10^{-3} joules cm^{-2} mb^{-1}).

REFERENCES

Batten, E. S., "A Model of the Seasonal and Latitudinal Variation of Zonal Winds and Temperatures in the Stratosphere Above 30 Km," *Memorandum* RM-4144-PR, The Rand Corporation, Santa Monica, Calif., June **1964**, 28 pp.

Bjerknes, Jakob A., "Extratropical Cyclones," *Compendium of Meteorology*, **1951**, pp. 577–598.

Buch, H. S., "Hemispheric Wind Conditions During the Year 1950, *General Circulation Project, Final Report*, Part 2, Contract No. AH19-122-153, Department of Meteorology, Massachusetts Institute of Technology, Cambridge, **1954**, 126 pp.

Bushby, F. H., and Timpson, Margaret S., "A 10-Level Atmospheric Model and Frontal Rain, "*Quarterly Journal of the Royal Meterological Society*, Vol. 93, No. 395, Jan. **1967**, pp. 1–17.

Edelman, W., *On the Behaviour of Disturbances in a Baroclinic Channel*, Contract No. AF61(052)-373 TN7, Research Division, German Weather Service, Offenbach, West Germany, Apr. **1963**, 35 pp.

Kraichnan, Robert H., "Inertial Ranges in Two-Dimensional Turbulence," *The Physics of Fluids*, Vol. 10, No. 7, July **1967**, pp. 1417–1423.

Leith, Cecil E., "Diffusion Approximation for Two-Dimensional Turbulence," *The Physics of Fluids*, Vol. 11, No. 3, Mar. **1968**, pp. 671–672.

Leith, Cecil E., "Numerical Simulation of Turbulent Flow," *Properties of Matter Under Unusual Conditions*, Interscience Publishers, New York, **1969**, pp. 267–271.

Lilly, Douglas K., "On the Application of the Eddy Viscosity Concept in the Inertial Subrange of Turbulence," NCAR Manuscript No. 123, National Center for Atmospheric Research, Boulder, Colo., **1966**, 19 pp., (unpublished manuscript).

Lilly, Douglas K., "Numerical Simulation of Two-Dimensional Turbulence," NCAR Manuscript No. 68-234, National Center for Atmospheric Research, Boulder, Colo., **1968**, 32 pp., (unpublished manuscript).

Manabe, Syukuro, and Hunt, Barrie G., "Experiments With a Stratospheric General Circulation Model: I. Radiative and Dynamic Aspects," *Monthly Weather Review*, Vol. 96, No. 8, Aug. **1968**, pp. 477–502.

Manabe, Syukuro, and Smagorinsky, Joseph, "Simulated Climatology of a General Circulation Model With a Hydrologic Cycle: II. Analysis of the Tropical Atmosphere," *Monthly Weather Review*, Vol. 95, No. 4, Apr. **1967**, pp. 155–169, [study M2].

Manabe, Syukuro, Smagorinsky, Joseph, and Strickler, Robert F., "Simulated Climatology of a General Circulation Model With a Hydrologic Cycle," *Monthly Weather Reveiw*, Vol. 93, No. 12, Dec. **1965**, pp. 769–798, [study M].

Matsuno, Taroh, "Numerical Integrations of Primitive Equations by Use of a Simulated Backward Difference Method," *Journal of the Meteorological Society of Japan*, Vol. 44, No. 1, Feb. **1966**, pp. 76–84.

Miyakoda, Kikuro, "Some Characteristic Features of Winter Circulation in the Troposphere and Lower Stratosphere," *Technical Report* No. 14, Grant NSF–GP–471, Department of Geophysical Sciences, The University of Chicago, Dec. **1963**, 93 pp.

Miyakoda, Kikuro, Smagorinsky, Joseph, Strickler, Robert F., and Hembree, G. D., "Experimental Extended Prediction With a Nine-Level Hemispheric Model," *Monthly Weather Review*, Vol. 97, No. 1, Jan, **1969**, pp. 1–76.

Oort, Abraham H., "On the Energetics of the Mean and Eddy Circulation in the Lower Stratosphere," *Tellus*, Vol. 16, No. 4, Nov. **1964***a*, pp. 309–327.

Oort, Abraham H., "On Estimates of the Atmospheric Energy Cycle," *Monthly Weather Review*, Vol. 92, No. 11, Nov. **1964***b*, pp. 483–493.

Peixoto, José P., "Hemispheric Humidity Conditions During the Year 1950," *Scientific Report* No. 3, Contract No. AF19(604)–2242, Department of Meteorology, Massachusetts Institute of Technology, Cambridge, Oct. **1958**, 25 pp.

Peixoto, José P., and Crisi, A. R., "Hemispheric Humidity Condition During the IGY," *Scientific Report* No. 6, Contract No. AF19 (628)–2408, Department of Meteorology, Massachusetts Institute of Technology, Cambridge, Nov. **1965**, 166 pp.

Phillips, Norman A., "Energy Transformations and Meridional Circulations Associated With Simple Baroclinic Waves in a Two-Level Quasi-Geostrophic Model," *Tellus*, Vol. 6, No. 3, Aug. **1954**, pp. 273–286.

Phillips, Norman A., "The General Circulation of the Atmosphere: A Numerical Experiment," *Quarterly Journal of the Royal Meteorological Society*, Vol. 82, No. 352, Apr. **1956**, pp. 123–164.

Platzman, George W., "The Spectral Form of the Vorticity Equation," *Journal of Meteorology*, Vol. 17, No. 6, Dec. **1960**, pp. 635–645.

Pond, S., Stewart, R. W., and Burling, R. W., "Turbulence Spectra in the Wind Over Waves," *Journal of the Atmospheric Sciences*, Vol. 20, No. 4, July **1963**, pp. 319–324.

Rasmusson, Eugene M., and Oort, Abraham H., "Mean Monthly General Circulation Statistics North of 10° S.: I. Mean Values of Meteorological Parameters," *ESSA Technical Report*, U.S. Department of Commerce, Boulder, Colo., **1970**, (to be published).

Saltzman, Barry, "Spectral Statistics of the Wind at 500 Mb," *Journal of the Atmospheric Sciences*, Vol. 19, No. 2, Mar. **1962**, pp. 195–206.

Saltzman, Barry, and Teweles, Sidney, "Further Statistics on the Exchange of Kinetic Energy Between Harmonic Components of the Atmospheric Flow," *Tellus*, Vol. 16, No. 4, Nov. **1964**, pp. 432–435.

Smagorinsky, Joseph, "On the Inclusion of Moist Adiabatic Processes in Numerical Prediction Models," *Berichte des Deutscher Wetterdienst*, Vol. 5, No. 38, **1957**, pp. 82–90.

Smagorinsky, Joseph, "General Circulation Experiments With the Primitive Equations: I. The Basic Experiment," *Monthly Weather Review*, Vol. 91, No. 3, Mar. **1963**, pp. 99–164.

Smagorinsky, Joseph, Manabe, Syukuro, and Holloway, J. Leith, Jr., "Numerical Results From a Nine-Level General Circulation Model of the Atmosphere," *Monthly Weather Review*, Vol. 93, No. 12, Dec. **1965**, pp. 727–768, [study S].

Smagorinsky, Joseph, and Staff Members, "Prediction Experiments With a General Circulation Model," *Proceedings of the International Symposium on Dynamics of Large-Scale Processes in the Atmosphere, Moscow, U.S.S.R., June 23–30, 1965*, Izdatel s'tvo "nauka," Moscow, **1967**, pp. 70–134.

Starr, Victor P., "Note Concerning the Nature of the Large-Scale Eddies in the Atmosphere," *Tellus*, Vol. 5, No. 4, Nov. **1953**, pp. 494–498.

Starr, Victor P., and White, Robert M., "Balance Requirements of General Circulation," *Final Report*, Part I, Contract No. AF19 (122)–153, Department of Meteorology, Massachusetts Institute of Technology, Cambridge, **1954**, pp. 186–242.

Teweles, Sidney, "Spectral Aspects of the Stratospheric Circulation During the IGY," *Planetary Circulation Project Report* No. 8, Massachusetts Institute of Technology, Cambridge, **1963**, 191 pp.

Wallace, J. M., "On the Role of [illegible] Meridional Motions in the Biennial Wind Oscillation," *Quarterly Journal of the Royal Meteorological Society*, Vol. 93, No. 396, Apr. **1967**, pp. 176–185.

Wiin-Nielsen, A., "On the Annual Variation and Spectral Distribution of Atmospheric Energy," *Tellus*, Vol. 19, No. 4, Nov. **1967**, pp. 540–559.

Wiin-Nielsen, A., and Vernekar, Anandu D., "On the Influence of the Mean Meridional Circulation on the Zonal Flow," *Monthly Weather Review*, Vol. 95, No. 11, Nov. **1967**, pp. 723–732.

[*Received July 22, 1969; revised October 17, 1969*]